Electric Propulsion Plasma Plume Simulation

Nicolò Massaccesi

TU Delft

Delft
University of
Technology

Challenge the future

Electric Propulsion Plasma Plume Simulation

by

Nicolò Massaccesi

in partial fulfillment of the requirements for the degree of

Master of Science
in Aerospace Engineering

at the Delft University of Technology,
to be defended publicly on Wednesday, December 18th, 2019

Student number: 4749626
Thesis committee: Prof.dr. L.L.A. Vermeersen
                   Ir. M.C. Naeije
                   Dr. A. Cervone
                   Dr. J. Laube

TUDelft Delft University of Technology

Abstract

In recent years the interest of the space community for electric propulsion has been rising thanks to the advantages that this technology offers. To ensure a correct integration on the spacecraft, it is important to be able to predict the behavior of the plasma plume generated by the thruster. Such plume could in fact damage spacecraft surfaces, produce parasite torques, etc. In order to simulate a plasma with contained computational power, the most used method in literature is the Hybrid Particle In Cell method.

In this research, a model of a Hall Effect Thruster is developed starting from on-ground measurements of the plasma. The model is built for a Hybrid Particle In Cell software. In order to validate the capability of the software to predict in-orbit plasma plume, a comparison with three space mission's set of data has been performed: Express-A, SMART1 and a satellite developed by OHB System. This thesis aims at proving that the Hybrid Particle In Cell software is capable of predicting the plasma plume reliably, given that this has been correctly set up. The research question leading the work is:

To which degree of precision can a hybrid particle-in-cell method as implemented by PICPluS predict in-orbit plume behavior when tuned with a non-empirical set of simulation parameters?

The thesis has been developed in cooperation with OHB System, a large system integrator leader in the sector, with proven experience in electric propulsion plasma plume simulation. The company provided supervision, all the hardware and software tools employed and an internal set of in-orbit data.

Contents

Symbols and abbreviations

Abbreviations

CEX	Charge Exchange (collision)
DSMC	Direct Simulation Monte Carlo
EP	Electric Propulsion
HET	Hall Effect Thruster
MCC	Monte Carlo Collision
PIC	Particle In Cell
RPA	Retarding Potential Analyzer
SPT	Stationary Plasma Thruster

Symbols

γ	Adiabatic coefficient	$[-]$
k_b	Boltzmann constant	$1.380649 * 10^{-23} \; \frac{\text{J}}{\text{K}}$
ρ	Charge density	$\frac{\text{C}}{\text{m}^3}$
J	Current density	$\frac{\text{A}}{\text{m}^2}$
λ_D	Debye length	m
w	Effective exhaust velocity	$\frac{\text{m}}{\text{s}}$
q	Electric charge	C
E	Electric field	$\frac{\text{N}}{\text{C}}$
ϕ	Electric potential	$\text{V} = \frac{\text{J}}{\text{C}}$
q_e	Elementary electric charge	$1.602177 * 10^{-19} \; \text{C}$
F	Force	N
m_0	Initial (spacecraft) mass	kg
θ_i	Inner ejection angle	$[°]$
σ_i	Inner ejection dispersion angle	$[°]$
B	Magnetic field	$\text{T} = \frac{\text{Ns}}{\text{Cm}}$
m	Mass	kg
n	Number density	m^{-3}
θ_o	Outer ejection angle	$[°]$
σ_o	Outer ejection dispersion angle	$[°]$
μ_0	Permeability of vacuum	$4\pi * 10^{-7} \; \frac{\text{H}}{\text{m}}$
ϵ_0	Permittivity of vacuum	$8.854187 * 10^{-12} \; \frac{\text{F}}{\text{m}}$
K	Poisson coefficient	$[-]$
p	Pressure	Pa
m_p	Propellant mass	kg
I_{sp}	Specific impulse	s
g_0	Standard gravity	$9.80665 \; \frac{\text{m}}{\text{s}}$
T	Temperature	$\text{K} = \frac{\text{eV}}{\text{k}_b}$
t	Time	s
v	Velocity	$\frac{\text{m}}{\text{s}}$

1

Introduction

In the past decades ion propulsion has often represented the best choice for spacecraft propulsion, especially for station keeping, but also as a main propulsion source. This is because ion propulsion, despite the lack of thrust power, can achieve very high specific impulses, one order of magnitude higher than chemical propulsion. This allows for a substantial reduction of the propellant mass needed by the spacecraft throughout its lifetime (Alenia-Laben and Spa 2005). Unfortunately, the implementation of such technology has some drawbacks as well.

One of the main issues of using ion propulsion is given by the interaction between the plasma generated by the engine and the spacecraft. The consequences vary from parasite torques (Korsun *et al.* 2005) to damaging of surfaces and sensible sensors, even when these are placed out of the engine's field of view. Other issues are related to communication disturbance and uneven spacecraft charging, the latter causing electrostatic arcs that could damage the components (Likar *et al.* 2009).

The importance of understanding the plasma plume behavior during the design phase of a spacecraft equipped with an ion thruster has then been motivated. To accomplish this task, the scientific community usually makes use of a numerical method called Particle In Cell (PIC). Despite numerous researchers have been using and validating the method, very few attempted to define a model that proved to be valid when validated against multiple sets of data.

The goal of this work is then to assess to which degree of precision and with which reliability a Hybrid Particle In Cell code can predict the in-orbit plume behavior of a plasma generated by an ion thruster. The goal is achieved by using on-ground sets of data in order to tune the software, while in-orbit data are used to validate the model.

In Chapter 2 a brief introduction to plasma dynamics is given. Moreover, the probes used in the literature to characterize a plasma are also described. In Chapter 3 the basic concepts of electric propulsion are mentioned. In particular, the thruster model that is the object of this study is described: the SPT100. In Chapter 4 the software used for this work is described. Specifically, PICPluS, a Particle In Cell tool and openPlumeEP, a ray tracing tool. Chapter 5 reports the phases of the work. Chapter 6 explains how the SPT100 has been modeled, including all the physical conclusions that were driven during the work. In Chapter 7 the results of the sensitivity analysis performed on the model are presented. In Chapter 8 the validation phase is described, proving the validity of the model described in Chapter 6. Finally, in Chapter 9 conclusions are drawn, wrapping up the work carried out throughout the thesis. Moreover, some hints on how to improve the work are given in Chapter 9.1.

2

Plasma Description

2.1. General Description

Plasma is the state of matter where the electrons are not bound to the atom nucleus. The process of generating a plasma from a gas is called ionization. A plasma can be fully ionized (no electrons are bound to the atoms) or partially ionized.

The mathematical description of a plasma is somewhat similar to that of a classical fluid, where the electrons and the atoms are treated as two separated species. Moreover, electromagnetic forces are now present among the particles. These forces have a radius of interaction that is much greater than that of the Van der Waals forces that drive a gas motion.

From a formal point of view, the electromagnetic fields (that might be generated by the plasma and that influence the motion of it) can be studied using the Maxwell's equations (Fleisch 2008):

$$\begin{cases} \nabla \boldsymbol{E} = \frac{\rho}{\epsilon_0} \\ \nabla \times \boldsymbol{E} = -\frac{\partial \boldsymbol{B}}{\partial t} \\ \nabla \boldsymbol{B} = 0 \\ \nabla \times \boldsymbol{B} = \mu_0 \left(\boldsymbol{J} + \epsilon_0 \frac{\partial \boldsymbol{E}}{\partial t} \right) \end{cases} \tag{2.1}$$

Where $\boldsymbol{E}$ and $\boldsymbol{B}$ are respectively the electric and magnetic field, ρ the charge density, $\boldsymbol{J}$ the current density and ϵ_0 and μ_0 the permeability and permittivity of vacuum, respectively. Starting from the first equation and imposing that $\boldsymbol{E} = -\nabla \phi$, the Poisson equation (Goebel and Katz 2008) can be obtained:

$$\nabla^2 \phi = -\frac{\rho}{\epsilon_0} \tag{2.2}$$

Here, ϕ is the electric potential. The Poisson equation relates then the electric potential to the charge density of a plasma and it is often used to compute the first from the latter.

When describing a plasma from a macroscopic point of view, the same quantities already in use for the gases can be used. In particular, the temperature (T) of a plasma could be measured, although it should be kept in mind that the temperature of the electrons could differ from that of the atoms (in which case, the plasma is said not to be in thermal equilibrium). In perfect gases, the particles tend to assume a Maxwell-Boltzmann distribution of velocities. For this reason, the temperature is usually measured in kelvin (or analogous). In a plasma, this condition might not be respected. For this reason, the plasma temperature is usually measured in electron-volts. In case of a Maxwell-Boltzmann distribution of velocities, there is a direct bound between the two:

$$T[\text{K}] = \frac{T[\text{eV}]}{k_b} \tag{2.3}$$

Here k_b is the Boltzmann constant.

Other macroscopic properties of a plasma are velocity ($\boldsymbol{v}$), number density (n) and current density ($\boldsymbol{J}$). These properties are bound by:

$$\boldsymbol{J} = qn\boldsymbol{v} = \rho\boldsymbol{v} \qquad (2.4)$$

Where q is the charge of a singe particle and ρ the charge density.

2.2. Probes

The plasma properties described until here can be measured using a specific set of probes. In this section, the most relevant for this work will be described.

2.2.1. Faraday Cup

A Faraday probe measures the ion current of a plasma. It is composed by a cup with a collector at the bottom. The collector is kept at negative voltage with respect to the plasma. When an ion enters the cup and hits the collector, a charge is transferred: the ion gets neutralized and the collector looses an electron. When several ions hit the collector, a current of electrons flowing towards the collector is generated. By measuring such current and the area of the collector, the ion current in the plasma can be determined. Some effort is usually put in the design of the cup in order to prevent the probe from disturbing the plasma flow and to limit secondary electron emission. In particular, secondary electron emission is a phenomena generated by highly energetic impinging ions on the collector. Such ions tend not only to absorb a single electron, but also to scatter a second one, generating twice the expected current. This problem could be overcome by a wise geometry of the cup or the introduction of an electric and magnetic field (Masoumzadeh *et al.* 2019). A scheme of a Faraday cup is shown in Figure 2.1.

2.2.2. Retarding Potential Analyzer

A Retarding Potential Analyzer (RPA for short) measures the ion energy distribution and its design is similar to that of a Faraday cup. It is composed by several grids. The first (screening grid) acts as a Faraday cage: it is grounded or kept at the plasma potential and prevents the electric field generated inside the probe to propagate externally. In this way, the probe is not intrusive (to a certain extent). The second grid is negatively charged, in order to repel the electrons. The third grid has a variable positive potential. The fourth grid is optional and is again negatively charged, in order to repel electrons that might have formed inside the probe or that might have passed the second grid. The ions are finally collected by a conductive material that measures the incoming current. Varying the potential of the variable potential grid and measuring the incoming current, the ion energy per electric charge distribution can finally be plotted (Bolton Ferda 2015). Note in fact that such a probe can not distinguish between a slow moving singly charged ion and a twice as energetically fast moving ion that is doubly charged due to the physics involved in the discrimination process. A scheme of an RPA probe is shown in Figure 2.2.

The working principle of the probe has been explained, but some additional observations are required in order to correctly model it. In particular, RPA probes tend to present angle-dependent and energy-dependent behaviors.

The first behavior is given by the shape of the probe. The ions that enter the probe need in fact to reach the bottom of it in order to be collected. This means that the effective area of the collector exposed to the ions is reduced. A representation of this phenomena is shown in Figure 2.3. Notice that ions and electrons that pass the screening grid and impact the probe lateral surface tend to recombine, so they are not detected by the collector (Korsun *et al.* 2005).

A consequence of this phenomena is that the measured current density is lower than the real one by a factor that is dependent on the ions direction with respect to the probe and the probe geometry. A second consequence concerns only the low energy ions. In fact, slow moving ions are likely to be formed in a different location than the fast moving ones, mainly due to collisions within the plasma.
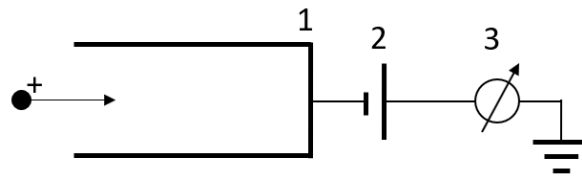
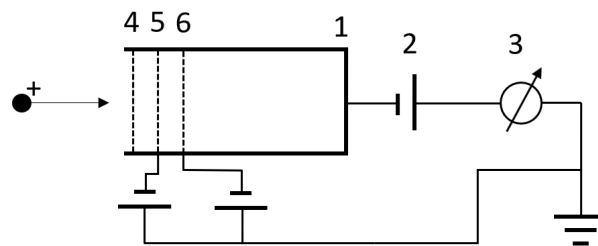Figure 2.1: Faraday cup schematics. 1: collector, 2:potential generator, 3: current sensor

Figure 2.2: RPA schematics. 1: collector, 2:potential generator, 3: current sensor, 4: floating grid, 5: electron repelling grid, 6: ion retarding grid
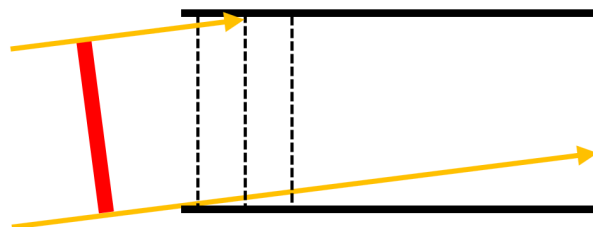

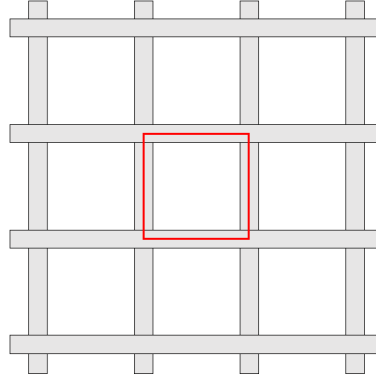Figure 2.3: RPA effective area exposed to the ion flow (in red)

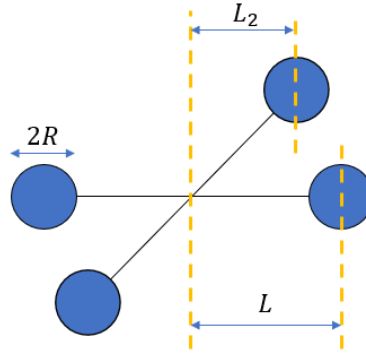Figure 2.4: Zoomed RPA grid seen from a direction perpendicular to it. In red the smallest grid element.

Figure 2.5: RPA grid seen from the side with its characteristic measurements

This means that, even when the probe is aligned with the average ion flux, some low energy ions are not detected, since they reach the probe from scattered directions. The measured current is then not only angle dependent, but also energy dependent.

The second behavior of an RPA probe is given by the transparency of the grids. In fact, not only the transparency of a single grid is angle dependent, but the alignment between the various grid layers plays an important role in determining how many ions reach the RPA collector. To understand why a grid is angle dependent, a simplified model is set up with the following assumptions:

1. The ions follow straight paths

2. The grid mesh is formed by perpendicular equally spaced wires forming square cavities

3. The grid mesh wires have a circular section

4. The ions are coming in a direction perpendicular to the axis of one of the two sets of wires (the horizontal ones, for instance)

Figure 2.4 shows the RPA grid when seen from a direction perpendicular to it. Due to its regularity, the transparency of the grid applies also to the smallest grid element (in red in the figure).
The transparency of the grid element can then be computed with:

$$t_0 = \frac{A_0}{A_{tot}} = \frac{(2L - 2R)^2}{(2L)^2} = \left(1 - \frac{R}{L}\right)^2 \tag{2.5}$$

Where A_{tot} and A_0 are the total element area and the element empty area at $0°$, L is the element half length and R the wires radius. The symbols convention is shown in Figure 2.5.

When the element is rotated around an axis parallel to one of the element sides (hereafter the horizontal side), its vertical side is reduced with $L_2 = L\cos\theta$, being L_2 the side dimension projected perpendicularly to the observation point. The new transparency will then be:

$$t_{eff} = \frac{4(L-R)(L_2-R)}{4L^2} = \left(1 - \frac{R}{L}\right)\left(\cos\theta - \frac{R}{L}\right) = \sqrt{t_0}\left(\sqrt{t_0} + \cos\theta - 1\right) \tag{2.6}$$

Where the ratio $\frac{R}{L} = 1 - \sqrt{t_0}$ has been derived from Equation 2.5. This formula of course looses validity when the incidence angle is higher than the critical $\theta_{cr} = \arccos\left(1 - \sqrt{t_0}\right)$ where the exposed area drops to zero. Despite the simplicity of the model, this shows that for geometrical reasons an angle dependency of the current measured by the probe is always present.

The last behavior of an RPA probe that is worth mentioning is the angle dependency of the ion energy detected. When in fact an ion enters the probe passing the screening grid, it is accelerated and repulsed by the other grids in a direction that is mostly perpendicular to the grids themselves. The retarding grid would then only act on the velocity component that is perpendicular to it. Decomposing the kinetic energy of a general ion:

$$K_z = \frac{1}{2}mv_z^2 = \frac{1}{2}m(v\cos(\theta))^2 = K\cos^2\theta \tag{2.7}$$

Here, K_z is the kinetic energy in the z direction (aligned to the probe axis) K the total kinetic energy, m the mass of the ion, v and v_z the ion velocity and its component in the z direction and θ the incidence angle (that is, the angle between the velocity and the probe axis). A correction factor would then need to be implemented.

2.3. Collisions

The particles of a plasma can collide in several different ways. In general, collisions can be of three different kinds:

1. In an *elastic collision* the kinetic energy is conserved

2. In an *inelastic collision* the kinetic energy is not conserved

3. In a *charge exchange collision* (CEX) there is a charge transfer: an electron (or more) moves between two atoms

For example, in the case of a plasma composed by solely Xenon atoms (a common propellant for electric thrusters), Table 2.1 can be built. Here, the charged particles are supposed to be accelerated by a potential ΔV (like in an electric thruster) before the collision. The resultant energy per electric charge of the products is given in the right side of the table. The neutral atoms are ignored. This table then shows the values that an RPA probe would measure.

A rough idea on the most probable collisions happening in a plasma is given by the fact that most common species collide more frequently and two species with higher relative velocity collide more frequently. Moreover, products obtained with the minimum expense of energy are more likely to form. To quantify the exact collision probability, the exact cross section of the collision should be experimentally measured.

Reactants		Products $\frac{E}{q}$				e^- transferred
		Xe^+	Xe^{2+}	Xe^{3+}	Xe^{4+}	
Xe^{2+}	Xe^+	$2\Delta V$	$\Delta V/2$			1
Xe^{2+}	Xe^+			$2\Delta V/3$		1
Xe^{2+}	Xe^+			$\Delta V/3$		2
Xe^{3+}	Xe^+		$3\Delta V/2, \Delta V/2$			1
Xe^{3+}	Xe^+				$3\Delta V/4$	1
Xe^{3+}	Xe^+	$3\Delta V$		$\Delta V/3$		2
Xe^{3+}	Xe^+				$\Delta V/4$	3
Xe^{3+}	Xe^{2+}		$3\Delta V/2$	$2\Delta V/3$		1
Xe^{3+}	Xe^{2+}	$2\Delta V$			$3\Delta V/4$	1
Xe^{3+}	Xe^{2+}	$3\Delta V$		$\Delta V/2$		2
Xe^+	Xe	0				
Xe^{2+}	Xe	$2\Delta V$				1
Xe^{3+}	Xe		$3\Delta V/2$			1
Xe^{3+}	Xe	$3\Delta V$				2

Table 2.1: Xenon plasma collisions with particles with charges up to $q = 4$. Electrically charged reactants are accelerated by a potential drop ΔV before the collision. The right side shows the products of the collision with their energy per charge. Neutral products are neglected (King 1998).

2.4. Quasi-neutrality & Debye Sheath

A particular condition in which a plasma could be is the so-called quasi neutrality. This condition is particularly important for the topic faced in this report, as explained in Section 4.2. The plasma is said to be in a quasi-neutrality state when the average charge density is null. This means that the positively charged particles are the same number of the negatively charged ones for a given volume. Of course, when the plasma is observed on a microscopic scale local charge accumulations arise. The quasi-neutral condition is the equilibrium state of the charges composing the plasma. Whenever a region would develop some net charge, the particles would redistribute among the plasma nullifying it (Piel 2010). The only area of the domain where this is not respected is a thin layer next to the surfaces. This layer is called Debye sheath (Goebel and Katz 2008). To understand the Debye sheath, consider having (for instance) a negatively charged surface immersed in a plasma. Positive charges would bend their trajectories towards it, while electrons would be repelled. A scheme of a Debye sheath is presented in Figure 2.6. This has two main consequences:

- Positive charges are accelerated towards the surface.

- Since a positive charge accumulates in the vicinity of the surface, the electric charge of the surface is shielded and will not be felt at distances greater than the so-called Debye length.

The first point implies that phenomena such as surface sputtering are amplified by the Debye sheath. The second point implies that the potential of a surface does not have an impact on the plasma flow, except for the very thin Debye sheath. This concept will be used in Section 6.3.

The Debye length can be computed with (Piel 2010):

$$\lambda_D = \sqrt{\frac{\epsilon_0 k_b T}{n_0 q_e^2}} \tag{2.8}$$

Here, ϵ_0 is the permittivity of vacuum, k_b the Boltzmann constant, T the temperature of the shielding specie, n_0 the number density of the undisturbed plasma and q_e the elementary charge. As mentioned, this measurement is important to assess where the quasi-neutrality condition is respected.
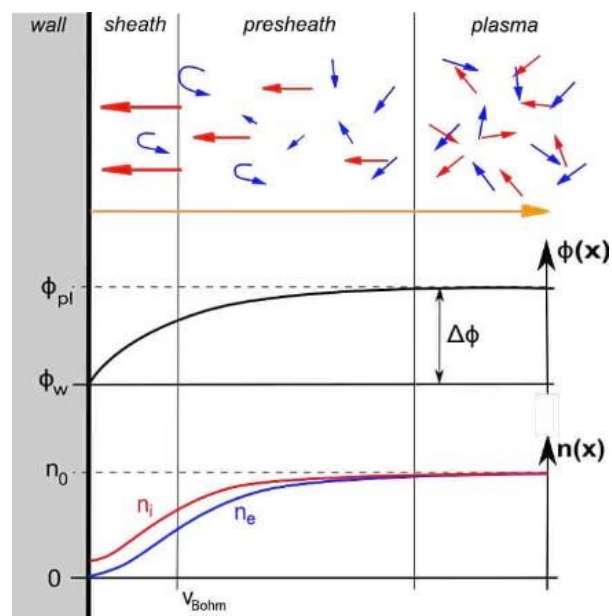
Figure 2.6: Plasma sheath (Kahnfeld 2015). The upper part represents the qualitative motion of ions (red) and electrons (blue). The middle part shows the electric potential drop $\Delta\phi$ between the plasma potential ϕ_{pl} and the wall potential ϕ_w. The bottom part shows the density (n) drop of ions and electrons (same color code as before).

3

Electric Propulsion

3.1. Electric Propulsion Basics

Space propulsion is the method that spacecrafts use to change their velocity. To do so, propellant mass (usually gas) has to be ejected from the spacecraft at a certain velocity. The relation between the spacecraft velocity change and the mass of ejected propellant is expressed by the Tsiolkovsky equation (Turner 2005):

$$\Delta V = w \ln \lambda \tag{3.1}$$

Where ΔV is the velocity change, $\lambda = \frac{m_i}{m_f}$ is the ratio between initial and final mass and w the effective exhaust velocity of the propellant. It is then clear that the velocity at which the propellant is ejected can be considered the efficiency of the propellant.

The traditional way of achieving this velocity is by using the chemical energy contained in the propellant itself. This technology (called chemical propulsion) allows to achieve high levels of thrust. Nonetheless, the specific energy available in the propellant (which is, the energy available to each kilogram of propellant) is then bounded to the specific energy contained in the propellant itself.

On the other hand, when electric propulsion is employed, the energy used to accelerate the propellant has another origin, usually the solar arrays. This means that a theoretically infinite specific energy can be given to the propellant (King 1998). Despite this, since the energy production rate of solar panels is very low, the propulsion system is power limited. This means that when high exhaust velocities are achieved, only a very low thrust is available. Decreasing the thrust corresponds in turn to decreasing the efficiency of the orbital maneuver, so an optimum point has to be searched (Hill and Peterson 1991). For this reason, the exhaust velocity of an electric thruster is usually not more than around 10 times higher than the one achieved by chemical propulsion.

3.2. Hall Effect Thruster

Numerous types of electric thrusters have been realized. In particular, the Hall Effect Thruster (HET) has been intensively employed in recent years, resulting often in the best design choice. This is because, despite its lower electrical efficiency and durability (with respect to gridded ion thrusters, for example), it holds a high thrust to power ratio with only a little reduction in specific impulse (Goebel and Katz 2008). As explained in Section 3.1 in fact, due to orbital mechanics reasons, having a too low thrust will ultimately result in diminishing the efficiency on the whole system.

A hall effect thruster (see Figure 3.1) is built around its circular discharge channel (Goebel and Katz 2008). The anode, which is also the gas inlet, is placed at the bottom of the channel. Within the walls of the channel (both inner and outer), magnetic coils are placed. A neutralizer placed outside the chamber serves as cathode. The relative position of anode and cathode generate hence an axial electric
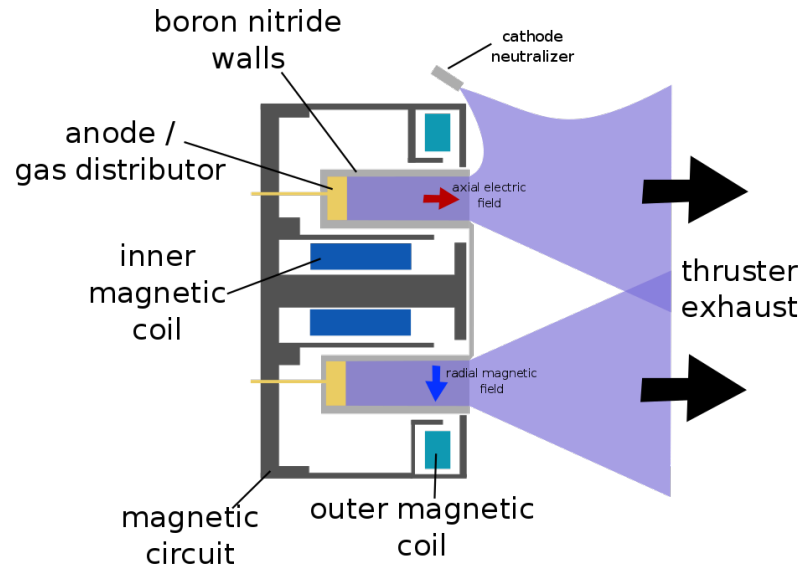
Figure 3.1: Hall effect thruster schematic (McWalter 2007)

field along the discharge channel, while the magnetic coils generate a radial magnetic field. Part of the electrons emitted by the cathode are attracted into the discharge channel, where they generate a Hall current. The electrons are in fact accelerated in the circumferential direction by the Lorentz force:

$$\boldsymbol{F} = q(\boldsymbol{E} + \boldsymbol{v} \times \boldsymbol{B}) \tag{3.2}$$

Here, $\boldsymbol{F}$ is the force applied to the electrons, q the electric charge, $\boldsymbol{v}$ the electron velocity and $\boldsymbol{E}$ and $\boldsymbol{B}$ the electric and magnetic fields, respectively.

The fast moving electrons impact with the incoming neutral gas, ionizing it. The ions react then to the electric field and get accelerated axially. The cloud of electrons emitted by the cathode that did not get attracted into the discharge channel will mix with the incoming ions and neutralize the plasma. For this reason, the plasma generated by a Hall effect thruster is often considered quasi-neutral (Goebel and Katz 2008).

Among all the Hall effect thrusters available, this work is focused on the analysis of one particular model: the Stationary Plasma Thruster-100 (SPT100). A picture of this model is shown in 3.2. This particular thruster uses xenon as propellant and has an outer diameter of the chamber of $100mm$ (hence the name). Table 3.1 shows the operational point of the thruster considered for this study.

Thrust	80 mN
Current	4.33 A
Mass flow	5.52 $\frac{mg}{s}$
Discharge voltage	300 V

Table 3.1: SPT100 Working conditions

Figure 3.2: Stationary Plasma Thruster family. The SPT-100 is at the top left corner (NASA/Glenn Research Center 1997).

4

Simulation Software

The task of simulating the behavior of a plasma is not trivial. Inside a plasma in fact long range forces are present, which are difficult to model with a classic solver based on some variation of the equations of Navier-Stokes. On the other hand, a fully kinetic simulation (where every particle is simulated independently) would require a way too vast computational load. Instead, the most commonly used technique to simulate a plasma is the Particle In Cell method (PIC). This method is briefly described in Section 4.1. Moreover, the particular software used for this study is described in 4.2.

Especially in the industrial world, approximate but quick solutions are often preferred over slow but exact ones. This is particularly true during the preliminary design phase of a product, but holds for other situations as well. In the context of this study, Particle In Cell simulations (both full PIC and Hybrid) are sometimes judged to be too slow. For this purpose, an approximate method has been developed by the scientific community: the ray-tracing method. During this study, a particular ray-tracing software has been used, and it is described in Section 4.3.

4.1. General Principles

The idea of the PIC method is to simulate the average behavior of the particles, without the eager to simulate every single one. To do so, the particles are grouped in superparticles and the domain is split in a finite mesh. Instead of computing the interactions, the particles' charge is deposited on the mesh nodes with a certain mapping function and the interaction is computed between the mesh nodes. The resulting forces are then mapped back to the particles. Finally, in the most common variant of the PIC, the Hybrid PIC, the electrons are not simulated like single particles but as a fluid.

4.2. PICPluS

In particular, the work described in Chapter 5 has been carried out with PICPluS (Particle In Cell Plume Simulator), a PIC code developed by SITAEL S.p.A (Alessandro Vicini 2018). In this chapter, a brief description of this software is given. This particular program has been selected because of the wide experience gathered throughout the years by the OHB engineers. This ensured a much quicker learning process.

PICPluS is a Hybrid PIC code capable of simulating the plasma generated by a source such as a Hall effect thruster. It can employ both the Direct Simulation Monte Carlo method (DSMC) and the Monte Carlo Collision method (MCC). Both of them use statistics to evaluate whether two particles are colliding instead of solving the exact collision interaction. Once again, this choice is taken to reduce the computational load. While the DSMC method simulates ions and neutrals (and their reciprocal interaction) at the same time, the MCC method first simulates the neutrals, handling the charged particles in a second moment. The idea behind the MCC method is that the influence of the ions on the neutral plume can be neglected (SIT 2016). A collision between charged and neutral particles with this method will then create slow moving ions without creating fast moving neutrals. This method has been recorded to

17

give results very close to the DSMC , with a current density difference not greater than 30% (Bondar *et al.* 2001). For this reason, this method is the only one applied during this study.

PICPluS is a hybrid PIC and it assumes the plasma to be quasi-neutral. The electrons are then modeled with an isotherm or an adiabatic model. Since the latter has been observed to better model a real plasma (Dannenmayer and Mazouffre 2013), this is the one that has been used throughout this work. When this is the case, the plasma potential can be computed from the full electron momentum equation:

$$m_e n_e \frac{d\boldsymbol{v_e}}{dt} = -n_e q(\boldsymbol{E} + \boldsymbol{v_e} \times \boldsymbol{B}) - \nabla p - n_e m_e v_{ei}(\boldsymbol{v_e} - \boldsymbol{v_i}) \tag{4.1}$$

Where m_e and n_e are the electron mass and number density, $\boldsymbol{v_e}$ and $\boldsymbol{v_i}$ the electron and ion velocities, $\boldsymbol{E}$ and $\boldsymbol{B}$ the electric and magnetic fields, p the pressure and v_{ei} the electron-ion collision rate. This equation is simplified using the following assumptions:

- Current-less flow: $\frac{d\boldsymbol{v_e}}{dt} = 0$

- Collision-less plume: $v_{ei} = 0$

- Un-magnetized electrons: $\boldsymbol{v_e} \times \boldsymbol{B} = 0$

- The electrons follow the ideal gas law: $p = n_e k_b T_e$, k_b being the Boltzmann constant and T_e the electron temperature.

- Adiabatic electron expansion: $T_e = T_0 \left(\frac{n_e}{n_0}\right)^{\gamma-1}$, T_0 and n_0 being reference values taken at the thruster exit and γ the adiabatic exponent.

By imposing the definition of the electric potential $\boldsymbol{E} = -\nabla\phi$ the following equation is obtained:

$$\phi_{qn} = \phi_0 + \frac{k_b T_0}{q} \frac{\gamma}{\gamma - 1} \left(\left(\frac{n_e}{n_0}\right)^{\gamma-1} - 1\right) \tag{4.2}$$

When computing the electric field, PICPluS does not solve the full Poisson equation (Equation 2.2) on the domain. Instead, the electric potential comes as a result of the addition between two fields. The first comes from the electric field driven by the physical surfaces and obtained by solving the linear Poisson equation ($\rho = 0$). The second is the potential drop driven by the electron expansion and computed with 4.2, where the quasi neutrality assumption is imposed, so that $n_e = n_i$ (n_i being the ion number density). The total electric field is then (SIT 2016):

$$\phi_{tot} = K\phi_{Poisson} + \phi_{qn} = K\phi_{Poisson} + \phi_0 + \frac{k_b T_0}{q} \frac{\gamma}{\gamma - 1} \left(\left(\frac{n_e}{n_0}\right)^{\gamma-1} - 1\right) \tag{4.3}$$

In this equation, K defines the predominance of the Poisson part against the quasi-neutrality part, and, with the name of *Poisson coefficient*, can be specified by the user. The other symbols have already been defined for Equation 4.2.

PICPluS is not capable of simulating the plasma inside the discharge channel, since a lot of phenomena happening there are not implemented in the current version (such as ionization processes). For this reason, the engine is modeled with a simple annular surface. The boundaries of the computational domain are then the thruster exit plane, the outer boundaries and the spacecraft surfaces. The boundaries electric condition can be of two types: Dirichlet or Neumann. With a Dirichlet condition, the potential of the plasma on that specific surface can be specified, while with a Neumann condition the gradient of the potential can be imposed to be zero. These conditions are relevant only for the calculation of the potential computed via Poisson equation.

PICPluS requires a wide range of other parameters in order to work. Table 4.1 shows the most important ones.

Parameter	Notes
Thruster Parameters	
Location and direction	
Internal and external radius	
Total mass flow	
Applied voltage	
Ionization efficiency	
Acceleration efficiency	Possibility to specify a distribution
Doubly charged ions percentage	
Temperature	Per every species
Mean radius and standard deviation	Per every species
Mean internal angle and standard deviation	Per every species
Mean external angle and standard deviation	Per every species
Environment parameters	
Background pressure	
Background temperature	
Electron adiabatic exponent	
Poisson coefficient	
Reference electron temperature and density	At chamber exit
Boundaries parameters	Per every boundary
Temperature	
Surface potential	
Boundary condition (Dirichlet or Neumann)	
Numerical parameters	
Number of steps	
Time step	
Time steps before probes data collection	

Table 4.1: PICPluS parameters

Here, the *ionization efficiency* is the percentage of propellant that gets ionized while the *acceleration efficiency* the fraction of potential difference that effectively accelerates the ions. For the latter property, two possible distributions can be adopted instead of a single scalar number: an angle dependent distribution and a mass dependent distribution. The particles are injected in the domain with an angle with respect to the axial direction that is dependent on the radial position of injection. Such angle is taken randomly from a Gaussian distribution with average and sigma linearly interpolated from the inner and outer ones (that are specified among the input parameters).

4.3. openPlumeEP

OpenPlumeEP (Zitouni *et al.* 2018) is a ray-tracing tool capable of computing plasma-spacecraft interactions when these take place at sufficient distances. Such distance is usually taken at $1m$. After this point, in fact, particles can be assumed to travel in straight lines without many collisions involved. This implies that the ion energy will remain constant for a certain angle from the thruster direction, while the current density will decrease with the rule:

$$J(r) = J(r_0)\frac{r_0^2}{r^2} \tag{4.4}$$

Where r is the distance from the source, r_0 a reference distance from the source, J the current density and J_0 the current density at r_0. The tool then takes as an input current density and ion energy angular distributions at a fixed radius and projects them to the spacecraft surfaces. Plasma-spacecraft

interactions are then computed, such as parasite forces and torques and surfaces material sputtering and contamination. Note that in order to compute the applied forces (and torques) the energy accommodation coefficient of the ions on the surface should be specified (that is, how much of the ion kinetic energy is transferred to the surface). For the purpose of this paper, this coefficient will always be set to 1 (fully inelastic collision), as indicated in the manual (Zitouni *et al.* 2018).

OpenPlumeEP has proved to be capable of computing the required values to a good degree of approximation and is computationally much faster than PICPluS. This tool has been employed during this thesis for a validation case, as explained in Section 8.3.

5

Work Description

In this chapter the actual work carried out during the thesis is described. In Section 5.1 the available tools are examined, while in Section 5.2 the phases of the research are presented.

5.1. Tools & Data

All the tools (software and hardware) used during the research have been provided by OHB.

The hardware tools comprise an office workstation used for general purposes and minor simulations and a server with superior computation capability. The latter have been used for the heaviest simulations. Due to the higher number of cores (20 physical), more simulations could be launched in parallel.

The software tools consisted in a license of PICPluS (see Section 4.2) and a license of openPlumeEP (Zitouni *et al.* 2018). Gmsh has been selected as a meshing tool. Python scripts have been vastly implemented for post and pre-processing. Paraview has been used for some results representation.

Four sets of on-ground data are available. The first three have been produced by a test facility hereafter named Test-Facility for OHB, where the thruster operational point is the same of the OHB-sat mission mentioned later. The three sets only differ in chamber background pressure. Current density and ion energy distributions are available. In particular, the first set contains a full solid-angle distribution of current density, while all the other data are taken only in a single plane. The second set has been produced by King (King and Gallimore 1998), and has a similar operational point to the Express-A missions (a series of geostationary communications satellites and part of the Express network of satellites (Korsun *et al.* 2005)). Current density and ion energy distributions are available. A quick recap of these sets is shown in Table 5.1.

Source	Set	Environment pressure
Test-Facility	Test-1	$\approx 1 * 10^{-3}$ Pa
Test-Facility	Test-2	$\approx 1 * 10^{-3}$ Pa
Test-Facility	Test-3	$\approx 5 * 10^{-3}$ Pa
King	MBMS	$6.67 * 10^{-3}$ Pa

Table 5.1: On-ground sets of data

Three sets of in-orbit data are available. The first set comes from the Express-A mission and consists in RPA signals and current density distributions during the thruster firing. The second set comes from the SMART-1 mission and it consists in the RPA signal measured in one specific point of the spacecraft. Finally, data from an OHB satellite are available (hereafter referred to as OHB-sat). The last data report the parasitic torques generated by the propulsion system. A recap of the in-orbit data sets is available

in Table 5.2.

Source	Current density	RPA signal	Parasite torques
Express-A	Distribution	Distribution	
SMART-1		Punctual	
OHB-sat			Distribution

Table 5.2: In-orbit sets of data

5.2. Phases of the Research

Hereafter a brief description of the research phases is presented.

5.2.1. PICPluS Training

As a first step the main simulation tool, PICPluS, has been examined. This required not only to simply read the instruction manual, but also to get confident with the software and to understand the meaning of each parameter, both in a physical and computational way. No official training on the software was available, but OHB experience helped during this phase.

5.2.2. Gmsh Training

Gmsh has been selected to mesh surfaces and volumes. The choice was based on the fact that Gmsh is arguably the most common free meshing tool available, and hence the better documented. Such tool has been used to generate 3D mesh inputs for PICPluS and 2D mesh inputs for openPlumeEP.

Most of the effort in this phase has been put to generate a good 3D mesh for PICPluS. It is in fact very important to control with accuracy the size of the cells in the various areas of the domain. As a requirement, the cells should be:

- Not too big, in order to increase accuracy. The PIC technique assigns in fact a value of the electric field to each mesh node and assumes a certain artificial distribution inside the cell. Hence the smaller the cells, the smaller the approximation error made by the PIC technique.

- Not too small, since the smaller the cells, the higher the number of cells, the higher the computational load required to solve the interaction between all the cells. Moreover, the statistics applied by the software inside the cells becomes poor when the number of particles per cell drops.

Moreover, while dimensioning the cells, it should be remembered that the most critical zones are those where the gradient in electric field is higher. It is in fact in those points that only a well refined mesh could capture the correct electric field distribution. Finally, since during experiments on-ground the thruster and the probe are as far as possible from other surfaces, only the thruster itself has been inserted in the computational domain. By extension, the same geometry has been used during in-orbit simulation cases as well, since the spacecraft surfaces are also believed to have little impact on the regions of the plasma of interest.

After some iterations, a good solution has been found. The domain is divided in rings of increasing outer radius and length and decreasing inner radius. For every ring, an increasing minimum cell size is assigned. The innermost ring is coincident with the thruster exit. This way, the most refined cells will be at the chamber exit, with a decreasing refinement approximately following the ion flow. Seven rings have been used in the final version of the mesh, since that number turns out to provide a smooth transition between the rings. A schematic example is shown in Figure 5.1.

5.2.3. PICPluS Study

Most of the effort throughout the thesis has been put in this phase. This consisted in launching simulations with different numerical parameters and evaluating the impact of each one. The available plasma data were used to tune the software in order to simulate a plasma generated by an SPT100.
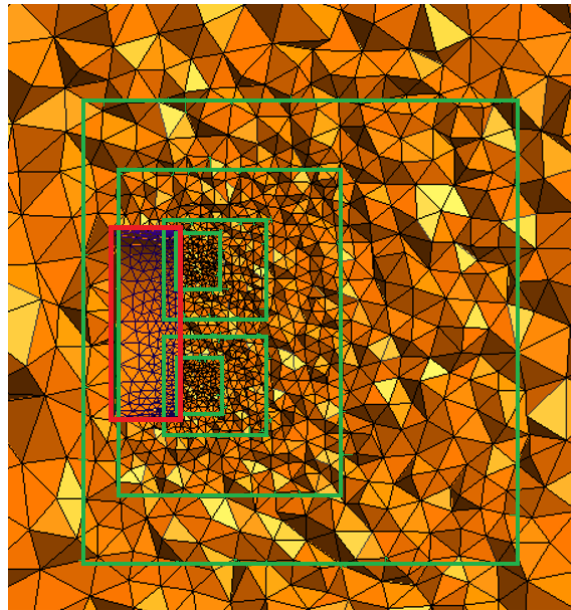
Figure 5.1: Mesh refinement areas. In red the thruster position. Some of the refinement rings (or cylinders) are highlighted.

This has been achieved by comparing the results of the software with the on-ground data available. In particular the Test-Facility data set Test-1 (see Table 5.1) have been chosen to be the one used for the tuning due to its completeness, but constant comparisons with the other sets have been also performed.

During this phase, the physical meaning of each choice has been considered. A detailed insight of this phase's results is given in Chapter 6.

5.2.4. Validation & Sensitivity Analysis

The final steps of the research implied a validation of the model using in-orbit data coming from three independent sources: Express-A, SMART1 and OHB-sat. This final phase served to assess that, after a tuning phase performed using solely on-ground data (that are usually available in a design phase) the software would have been capable of predicting the plume behavior in space, which is the normal operating condition of the thrusters.

6

Model Development

After the study phase described in Subsection 5.2.3, some properties of the plasma plume generated by an SPT100 have been observed. These properties are described in this chapter.

6.1. Low Impact Parameters

After a brief study, some parameters have been found to have only little impact on the output of the software. Here, only the ion energy and current density distributions have been taken into consideration. The software also outputs other values, such as the thrust and the current flowing in the engine. Nonetheless, these values have been mostly ignored during the tuning. While the former is in fact already hidden in the current density and ion energy distributions, the latter does not correspond to the current measured by the sensors inside the engine, as will be explained in Section 6.4. The low impact parameters include:

- Flow temperature (both neutrals and ions)

- Neutrals thruster exit angles

- Percentage of doubly charged ions

These parameters have not been explored during this study to limit the variables set dimension and respect the time constraints. As mentioned in 9.1, these might be taken into consideration in case of a future work on the topic.

In order to better understand the selection process for the mentioned parameters, the following section shows the case of the percentage of doubly charged ions. The other parameters have been similarly examined.

6.1.1. Percentage of Doubly Charged Ions

According to the literature, a value around 10% (King and Gallimore 1998) or $20\% - 25\%$ (Manzella and Sankovic 1995) is considered acceptable. A sensitivity analysis shows the impact of the parameter on the average ion energy and current density distributions, as reported in Figure 6.1.

As it can be seen, the impact of the studied parameter in the surrounding of the suggested value is marginal, accounting for a maximum of 13% around the centerline for the current density. The thrust for these cases has also been computed, as shown in Table 6.1. As shown, the variation in the thrust also accounts only for a few percentage points. For these reasons, this parameter has been classified as low impacting.
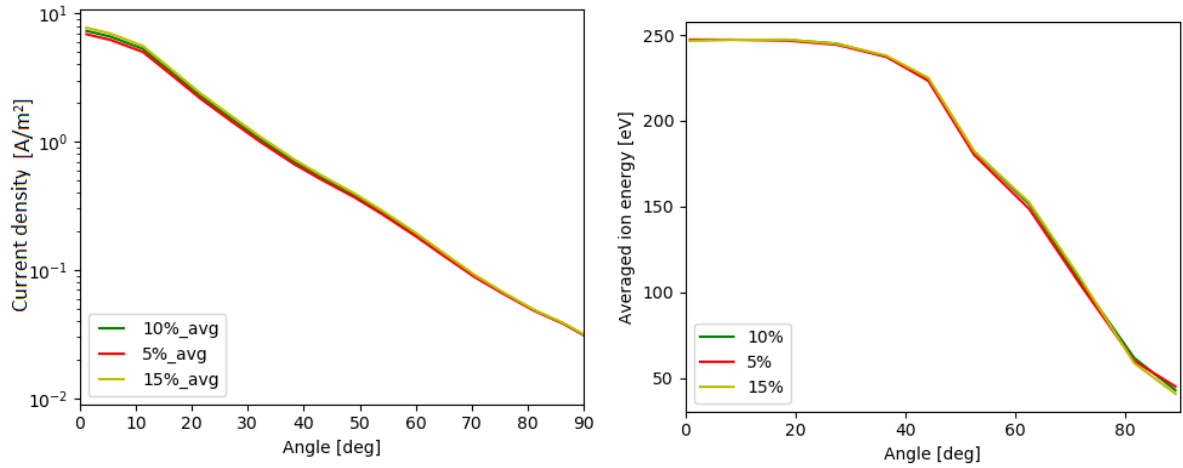
Figure 6.1: Impact of the percentage of doubly charged ions on the average ion energy and current density distributions

Percentage of Doubly Charged Ions	Thrust
5%	78.1N
10%	79.7N
15%	81.2N

Table 6.1: Effect of the percentage of doubly charged ions on the thrust

6.2. Boundary Conditions

In PICPluS two kinds of boundary conditions are possible: Neumann and Dirichlet. Using a Dirichlet condition means pinpointing the potential to a specific homogeneous value throughout the surface. On the other hand, specifying a Neumann condition implies imposing the derivative of the field perpendicular to the surface to be null. The physical meaning to this is that the Dirichlet condition is good to model a conductive material. The charge is in fact equally spread throughout the surface with no local accumulation. On the other hand, a Neumann condition imposes the gradient to be only parallel to the surface. This is a good model of an insulating surface. The SPT100 (Figure 6.2) is composed by concentric layers of different materials. From the innermost to the outermost, the following layers are recognizable:

1. The inner gray metal structure, which is grounded

2. The inner white ceramic coating, which is an insulator

3. The chamber exit

4. The outer white ceramic coating, which is again an insulator

5. The outer gray metal structure, which is again grounded

It is then clear that the various layers should be separated in the geometry and different boundary conditions should be assigned to each layer. Regarding the external boundaries, a Dirichlet condition of null potential has proven to be better than a Neumann one, which tends to keep the potential too high at high distances from the thruster.

6.3. Poisson Coefficient

A small study has been performed in order to understand the physical meaning and the impact of the Poisson coefficient. As mentioned in Section 4.2, this coefficient determines the impact of the Poisson equation in the computation of the electric potential. It appears that solving the non linear Poisson equation (Equation 2.2) would be useful only for a fully kinetic code. Since PICPluS does not simulate
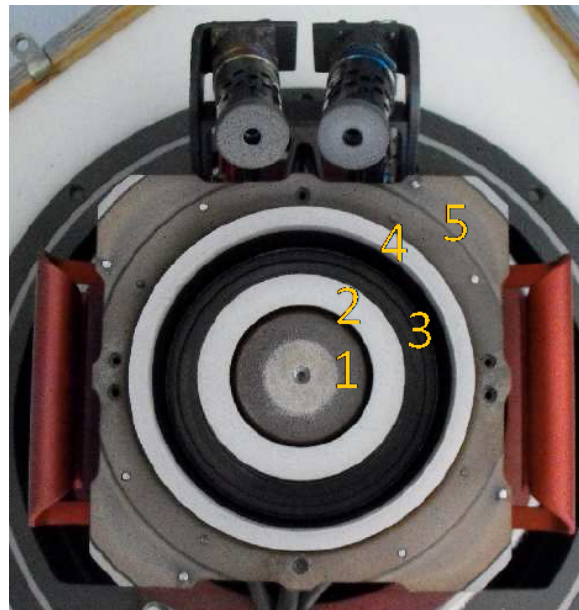
Figure 6.2: SPT100. 1,5: metallic structure, 2,4: ceramic layers, 3: thruster exit (Confidential 2009)

the electrons independently but instead assumes a condition of quasi neutrality, the solution of this equation would in fact have only little meaning. To be clear, the charge density should always be null, and hence the Poisson equation should be reduced to its linear form. This solution does not seem to give results backed by observations. For instance, Dannenmayer (Dannenmayer and Mazouffre 2013) measured the electric field generated by a PPS1350 thruster (which is similar to an SPT100) measuring a shape clearly not circular (see Figure 6.3), while, after a short transient area, the electric potential generated only by the Poisson equation would converge to a semi-circular shape (Figure 6.4).

This suggests that the potential of the surfaces should not influence the plasma potential in a meaningful way. This is backed by the Debye shielding reasoning (see Section 2.4). According to that, in fact, the potential of the surfaces should have an impact only in the proximity of the surfaces themselves. It appears then that the Poisson part of the electric potential computed by PICPluS should be ignored.

Some simulations have investigated the impact of the phenomena on the model. As shown in Figure 6.5, the most important impacts of this number are the position of the inflection point in the current density distribution and the low angle average ion energy. As shown in the same figures, the impact seems to be counterbalanced almost perfectly by a decrease in ion energy of $40V$.

The outcome of this investigation is then that the Poisson solver should be ignored. Other available software (such as SPIS) allow taking into account the surfaces charging only in the proximity of the surfaces. This approach seems more exact than that available with PICPluS. When such approach is implemented, the thruster model described in 6.2 could be used. When the surface potential is not taken into account the thruster surfaces model has no impact on the results.

6.4. Currents in the Engine

An information that is usually available in the measurements is the amount of current provided to the engine. In order to assess a correlation between this value and the current detected by the RPA and Farady probes during the plasma plume characterization, a brief study on the currents flowing through the engine has been performed.

When the thruster is working, xenon gas is emitted from the anode placed at the base of the discharge chamber. Under pressure forces, the xenon starts moving towards the end of the discharge
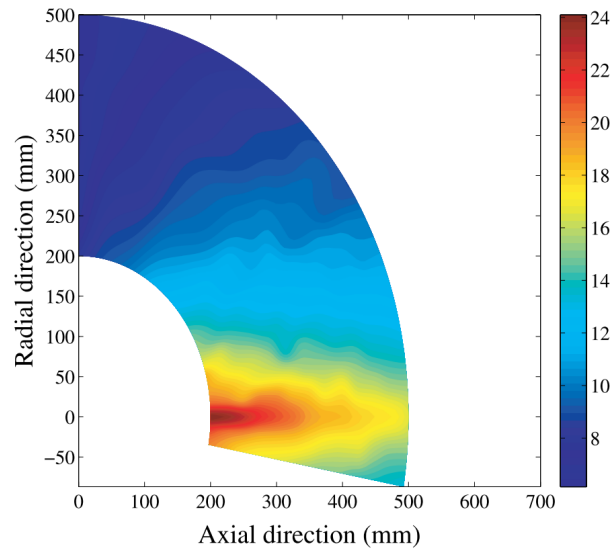
(a) Plasma potential

Figure 6.3: Dannenmayer's measurements of the electric field on a PPS1350 (Dannenmayer and Mazouffre 2013)
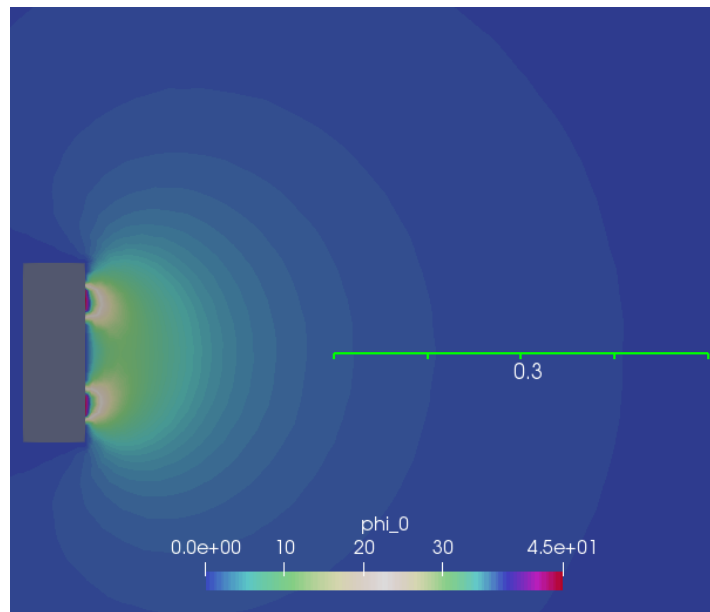
Figure 6.4: Plasma potential computed by PICPluS when only the Poisson equation is taken into account. To facilitate the comparison with Figure 6.3, the ruler (green line) indicates the area from $0.2m$ to $0.5m$
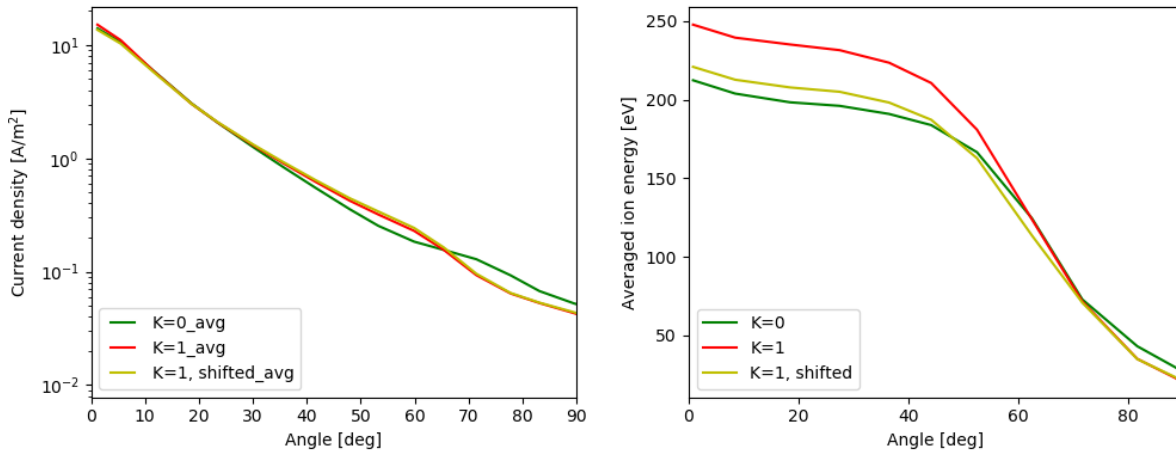
Figure 6.5: Impact of the Poisson coefficient K on the current density (left) and ion energy (right) distribution. When *shifted* is mentioned, the ions have been decelerated by $40V$. All y values have been scaled by a confidential factor meant to protect OHB sensible data.

chamber. At the same time, electrons are generated by the cathode. Due to the potential difference between anode and cathode, part of the electrons are attracted inside the discharge chamber. The exact percentage is unknown, but some reasoning could be made nonetheless.

Following the nomenclature in Figure 6.6 and imposing that $B = \alpha A$ (where $\alpha < 1$), the following equations can be written:

$$\begin{cases} A = B + C = C + D \Rightarrow D = B = \alpha A \\ C = A(1 - \alpha) \end{cases} \tag{6.1}$$

Note that the first equation comes from the current conservation at the node ABC and from the reasoning that for every ion generated an electron is also formed (D). These electrons will add to those entering the chamber (C) and be collected by the anode (A).
This implies that:

- The plasma is quasi-neutral

- The amount of current (both ionic and electric) that gets measured by the probes is smaller than that passing through the propulsion power unit

While the first consequence gives validity to the assumptions made in 4.2, the second one shows that there is no direct correlation between what is measured by the probes and the nominal current provided to the engine. The amount of electrons flowing back to the chamber is in fact unknown.

6.5. Ejection Angles

The first set of parameters studied are the ejection angles of the plasma. The real plasma will likely be ejected from the thruster exit plane with a very complex angular and velocity distribution depending on the radial position and on the circumferential position. On the other hand, PICPluS can approximate this only with a simple linear radius dependent distribution. As explained in Section 4.2, two angles and two sigmas have to be given.

A literature research highlighted a research by Manzella (Manzella 1994) that describes non intrusive measurements of the ion velocity distribution right after the chamber exit based on laser induced fluorescence. The data acquired do not cover the whole chamber exit, but clearly show a linear angle ejection dependency with the radius. This confirms that the simplified model employed by PICPluS is in fact a good approximation of the real plasma flow. Projecting such measurements to the inner and outer radii, the resulting inner and outer angles are shown in Table 6.2. Since the method employed only
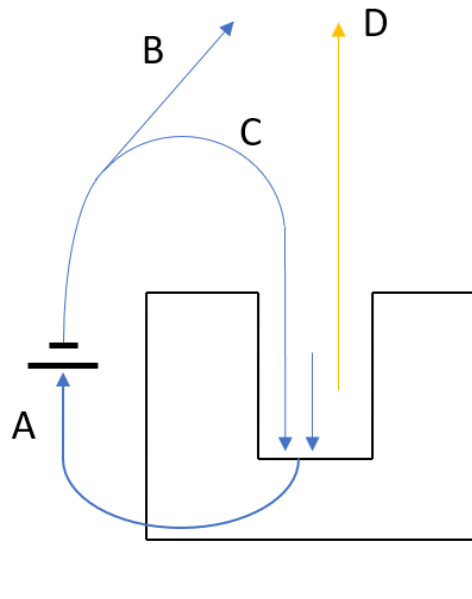
Figure 6.6: Balance of currents inside and outside the thruster. Electron currents in blue, ion currents in orange. **A** is the current passing through the thruster power unit, **B** the current that composes the plasma plume and **C** the current entering the discharge chamber. **D** is the ion current exiting the chamber.

measures the average velocity, no sigmas could be extracted from this work. Moreover, the available angles are not to be taken for exact due to the rough extrapolation technique performed. Finally, different sources seem to give different values for the angles, so their estimation has been performed ignoring the found values.

	Inner	Outer
Angle	2.29°	23.20°

Table 6.2: Ejection angles of the SPT100 according to Manzella measurements (Manzella 1994)

The starting point for the estimation of the ejection angle comes from another literature work. When the ion energy is plotted with respect to the angle from the thruster firing direction, at $1m$ the plot has roughly the shape of a Gaussian function, while at $0.5m$ the plot has a down-peak in the middle. This behavior has been detected by King (King 1998), and he suggests that this is a hint of the ions getting generated closer to the inner wall (Figure 6.7).

In his attempt to simulate an SPT100, Loureiro (Loureiro 2010) uses an inner angle of $-12°$ and an outer angle of $40°$. This has been the starting point for the ejection angles. To assess which exact values of angles better describe the real flow, a sensitivity analysis has been performed using arbitrary guesses for the unknown sigmas. The outer sigma is analyzed first. The greatest impact of this parameter is on the average energy, which is shown in Figure 6.8. It can be observed that having an angle that is too high keeps the energy at high levels even at high angles away from the thruster, while an angle that is too low makes the energy drop too quickly.

A similar impact can be attributed to the outer ejection angle (Figure 6.9). Moreover, this parameter has a strong impact on the position and strength of the inflection point in the current density curve (Figure 6.10).

The inner angle has a big impact only on the inflection point of the current density while the value is smaller than that of the outer angle (Figure 6.11). On the other hand, when the inner ejection angle becomes too wide, the particles shot from one side of the engine start influencing the other side of the plume. This generates double peaking shapes in the average energy distribution (Figure 6.12).
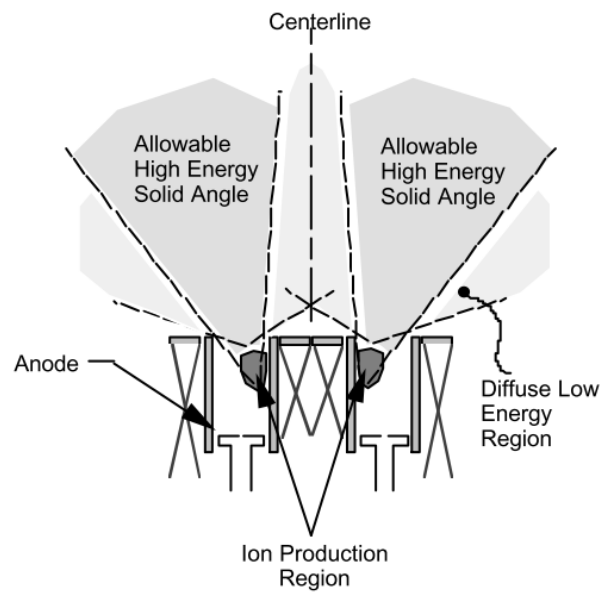
Figure 6.7: King's hypothesis on ionization bulk location (King 1998)
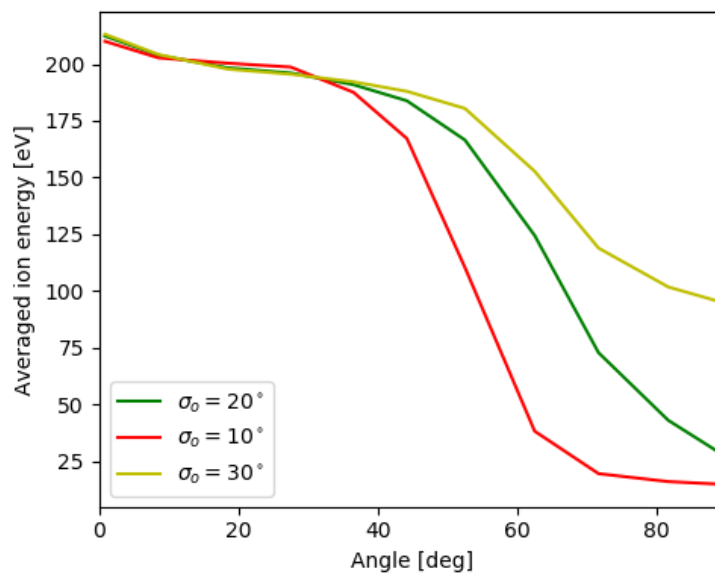
Figure 6.8: Outer sigma influence on the average ion energy. All y values have been scaled by a confidential factor meant to protect OHB sensible data.
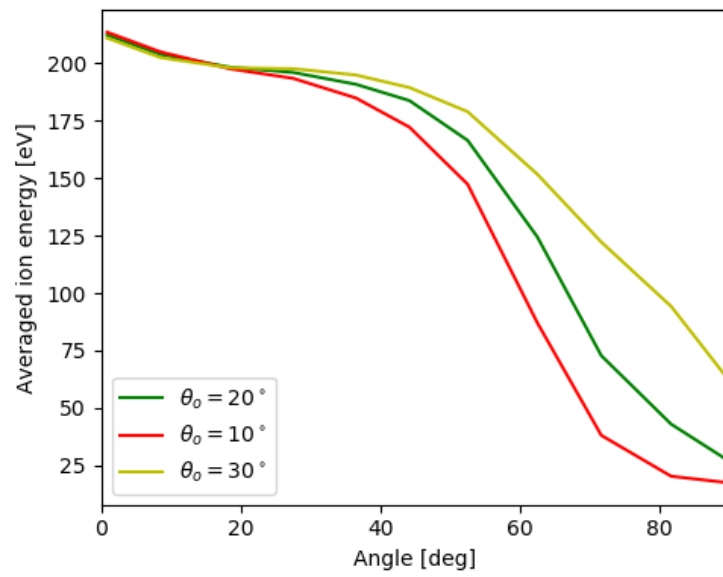
Figure 6.9: Outer angle influence on the average ion energy. All y values have been scaled by a confidential factor meant to protect OHB sensible data.
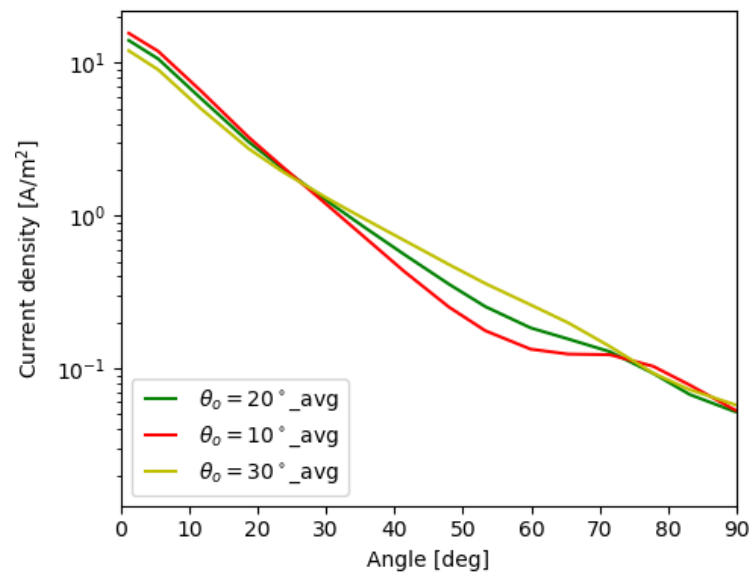
Figure 6.10: Outer angle influence on the current density. All y values have been scaled by a confidential factor meant to protect OHB sensible data.
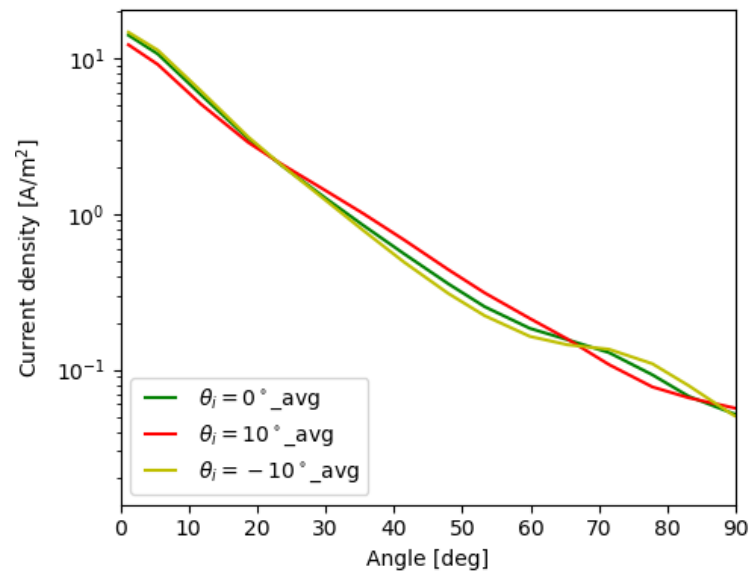
Figure 6.11: Inner angle influence on the current density. All y values have been scaled by a confidential factor meant to protect OHB sensible data.
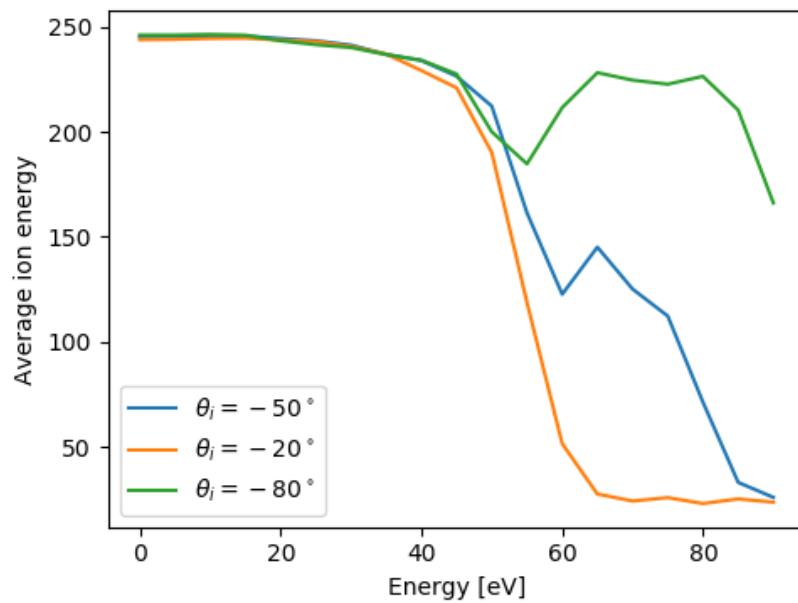
Figure 6.12: Inner angle influence on the average ion energy when the angle is too high. All y values have been scaled by a confidential factor meant to protect OHB sensible data.
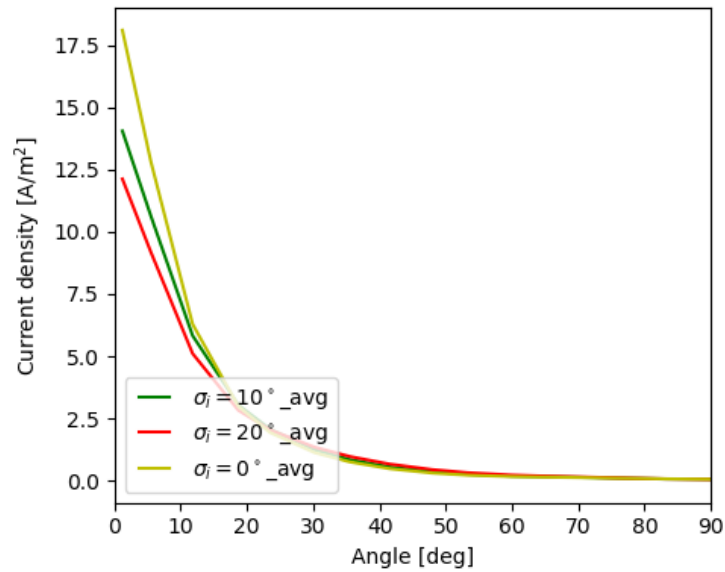
Figure 6.13: Inner sigma influence on the current density. All y values have been scaled by a confidential factor meant to protect OHB sensible data.

The internal sigma only presents this last behavior. It is then clear that the inner angles have indeed to be smaller than the outer. Finally, the inner sigma has a strong impact only on the centerline current density (Figure 6.13).

After a testing phase, a set of angles have finally been selected. The angles used are shown in Table 6.3. The similarity between these values and those found by Manzella (Table 6.2) gives confidence to the obtained results, since they were obtained with a completely independent technique.

	Inner	Outer
Angle	0°	20°
Sigma	10°	20°

Table 6.3: Ejection angles of the SPT100

6.6. Adiabatic Coefficient

As mentioned in Section 4.2, the electrons are modeled as an adiabatic fluid. In this context, an adiabatic coefficient has to be selected. According to gas kinetic theory, the adiabatic coefficient is a measure of how much energy goes into thermal energy (particle kinetic energy) and how much gets distributed to different forms of energy (vibrational and rotational). It is then strictly connected to the number of degrees of freedom of the gas with:

$$\gamma = 1 + \frac{2}{f} \qquad (6.2)$$

Here, f are the degrees of freedom of the gas and γ the adiabatic coefficient. A monoatomic gas would have $\gamma = 1.66$, while the lower boundary is represented by an isothermal process, where $\gamma = 1$. When electrons are considered, a first hypothesis is to consider them as monoatomic gas particles. Despite this, experiments tend to prove that a more accurate number would be much lower. This is caused by the fact that ionization and recombination processes increase the degrees of freedom of the electrons (Dannenmayer and Mazouffre 2013). Pinpointing a unique value for the adiabatic coefficient seems difficult, since this seems to change when different thrusters are tested (Dannenmayer and
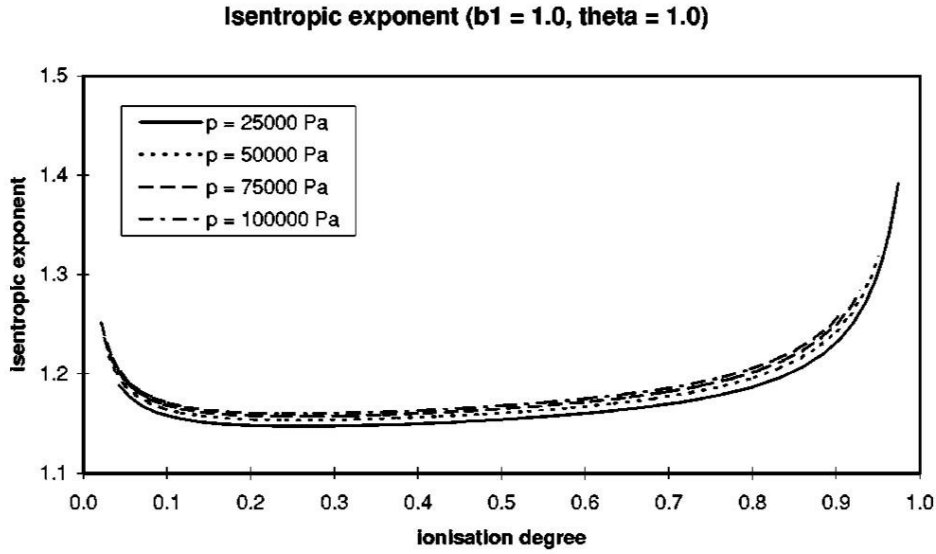
Figure 6.14: Adiabatic coefficient dependency on the ionization degree (Burm, K. T. A. L. *et al*. 1999)

Mazouffre 2013). A theoretical research shows indeed that the coefficient heavily depends on the ionization coefficient of the plasma as depicted in Figure 6.14. For this model a value of $\gamma = 1.33$ will be selected. This in fact is between the two values extrapolated in the literature (Dannenmayer and Mazouffre 2013), and is then considered a reasonable value. The impact of this coefficient on the resulting plasma properties has been assessed with a sensitivity analysis (see Chapter 7 for the complete study). As shown in Figure 6.15, the impact is limited, and hence no more effort has been put in determining the adiabatic coefficient. The figure shows in fact the variation of current density and average ion energy with the angle from the thruster at $1\mathrm{m}$ from the source in the case of two different adiabatic coefficients.

6.7. Discharge Chamber

What has emerged from the previous section is that the understanding of the phenomena happening inside the discharge chamber is very important in order to determine the ejected plasma properties. For instance, the exact location of ionization determines the kinetic energy of the ions at the chamber exit (potential drop between the two points). Since PICPluS, as explained in Section 4.2, requires an ion energy distribution at the thruster exit as an input, it is clear that this aspect of the discharge chamber has to be assessed.

6.7.1. Direct Measurements

Some measurements taken inside the discharge chamber are available in literature. These measurements are rare, since probing the plasma in a reliable way inside the chamber presents some challenges. In fact, not only the plasma is very hot and likely to alter the electric behavior of the probe, but being the discharge chamber usually very small, it is difficult to acquire measurements non intrusively. Nonetheless, Thomas et al. (Thomas *et al*. 2004), for example, used a non intrusive technique to measure the magnetic field and the Hall current inside their experimental thruster. The latter has a close resemblance to the SPT100, but these measurements should nonetheless be considered only indicative. The main results are summarized in Figure 6.16.

The figure shows clearly that the magnetic field is stronger near the exit, and the Hall current has a peak not too far from there. Moreover, the two are more concentrated on the inner side of the thruster. This suggests much higher exit angles at the outer wall than at the inner wall, once again proving the hypothesis in Section 6.5.
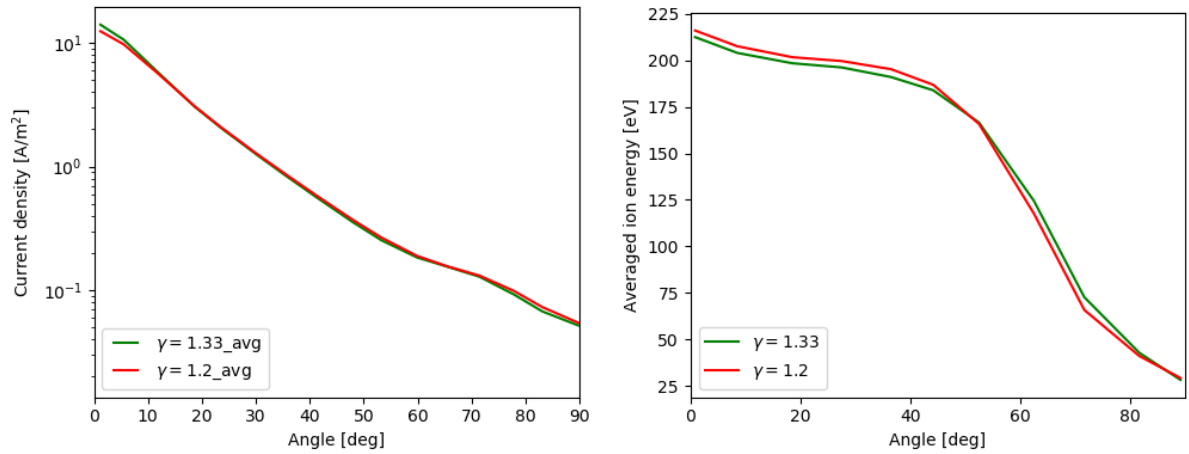
Figure 6.15: Sensitivity analysis on electron adiabatic coefficient: current density and average ion energy distributions. All y values have been scaled by a confidential factor meant to protect OHB sensible data.
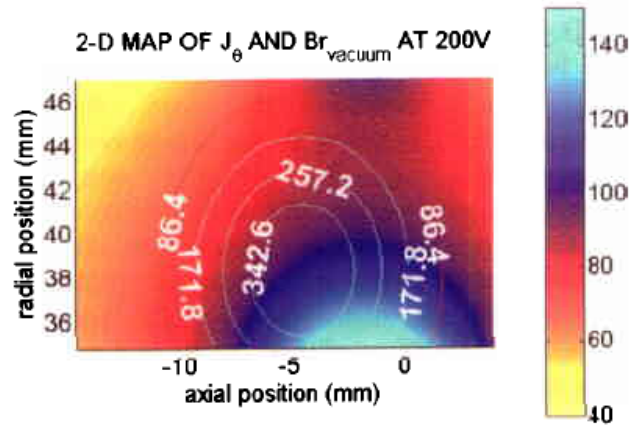
Figure 6.16: Magnetic field (shaded 2-D background) in $G = 10^{-4}T$ and average azimuthal drift (contours) in $\frac{kA}{m^2}$ (Thomas et al. 2004)
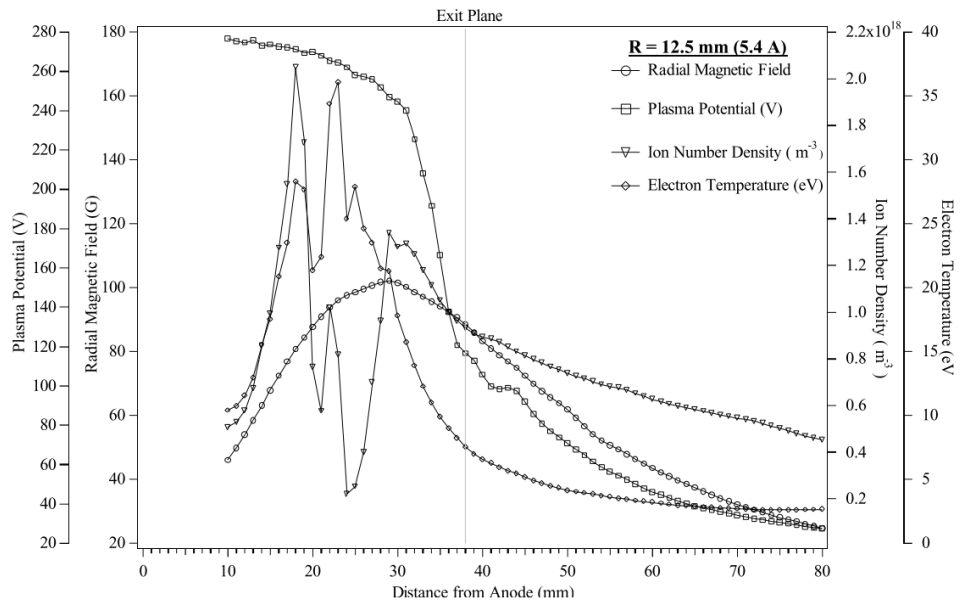
Figure 6.17: Plasma properties at the average chamber radius (Haas and Gallimore 2000)
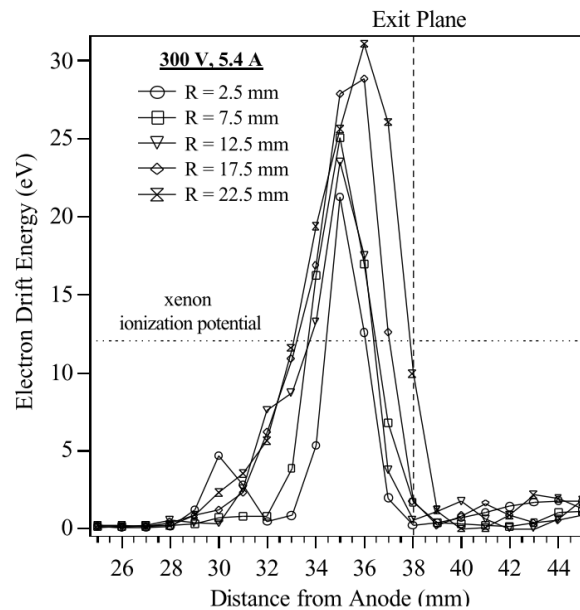
Figure 6.18: Electron drift energy axial profiles (Haas and Gallimore 2000)

A second source of measurements from inside the thruster comes from Gallimore et al. (Haas and Gallimore 2000). In his paper, a probe has been inserted in a working Hall thruster (once again, not an SPT100) and plasma potential, magnetic field, ion density and electron temperature data have been taken. Some of these data are shown in Figure 6.17 and Figure 6.18.

The first observation is that the magnetic field has its maximum near the chamber exit. Moreover, the other plots in the paper (not shown here since they carry little additional information) representing the measurements taken at different radii show that the maximum is located near the inner wall. This is in agreement with the measurement of Thomas et al. (Thomas *et al.* 2004).

The second observation is that the ion density has two peaks. This suggests that two bulks of ionization are present. In the paper this phenomena is pointed out, and the first (closest to the anode) is attributed to the electron temperature maximum, while the second (closer to the chamber exit) is attributed to the location of the maximum drift velocity.

6.7.2. RPA Readings

Another way to understand what is happening inside the discharge chamber is to analyze the retarding potential analyzer (RPA) measurements gathered at a certain distance from the thruster. Despite being indirect measurements, these are usually more trustworthy than the direct measurements inside the thruster. In fact, not only probes inserted in the chamber undergo a certain thermal stress that might alter the measurements, but the presence of the probe itself is very inclined to disturb the flow. Here, three data sets are analyzed: two coming from King's research (King 1998) and one from the Test-Facility.

King's Molecular Beam Mass Spectrometer

The first set of ion distribution measurements that will be analyzed are those obtained by King (King 1998). Instead of an RPA, he used a Molecular Beam Mass Spectrometer (MBMS), but despite the differences, they gather the same data. King itself proposes a description of the energy distributions that will be here briefly reported.

At small angles from the thruster firing direction, a long monotonically decreasing trace is present
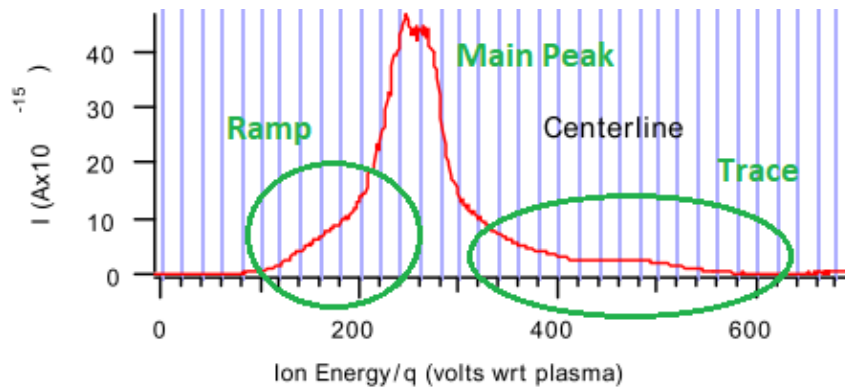
Figure 6.19: Ion energy distribution at the centerline at $0.5\ \mathrm{m}$ from the thruster (King 1998)
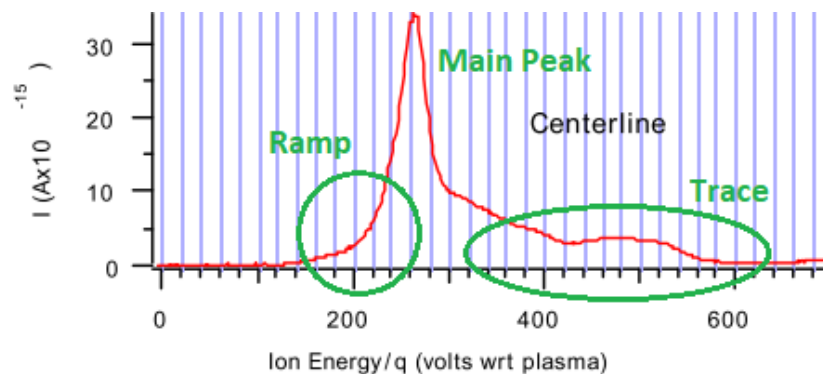
Figure 6.20: Ion energy distribution at the centerline at $1\ \mathrm{m}$ from the thruster (King 1998)

on the right of the main peak (Figure 6.19 and Figure 6.20). The main peak is generated by the bulk of ionization inside the thruster. The trace on the right side is generated by elastic collisions between singly and doubly charged xenon particles. The doubly charged particles would in fact have twice the velocity of a singly charged particle thanks to the greater force an electric field can apply to it. At the same time, the doubly charged particles would be slowed down. This effect is visible as a ramp on the left side of the main peak. As expected, while the main peak is positioned around $260\ \mathrm{V}$, the right-hand trace ends around $520\ \mathrm{V}$. This effect is more visible at $0.5\ \mathrm{m}$ from the thruster, while at $1\ \mathrm{m}$ the CEX products are more visible.

At intermediate angles, charge exchange (CEX) products become visible (Figure 6.21 and Figure 6.22). They are recognizable as a bump at twice the energy of the main peak. According to Table 2.1, for almost every collision with one of the products having twice the initial energy, a product with some other different energy is also generated. Since no other bump is visible, the origin must be the CEX interaction $\mathrm{Xe^{++} + Xe \Rightarrow 2Xe^{+}}$.

Already at intermediate angles but in a more evident way at high angles, the profile shows a shoulder on the left side of the main peak which could not be explained only with collisions (Figure 6.23 and Figure 6.24). King drives the hypothesis that this shoulder is generated directly inside the engine. The shoulder seems to position itself around $120\ \mathrm{V}$. The origin of this shoulder could be a second ionization bulk, the existence of which has already been suggested in Section 6.7.1.

King's RPA
King performed measurements using an RPA as well. Unfortunately, those are affected by a high uncertainty level. Nonetheless, the left shoulder already detected with the MBMS is still visible (Figure 6.25). The energy values of the main peak and the side shoulder seem to match with those detected with the MBMS.
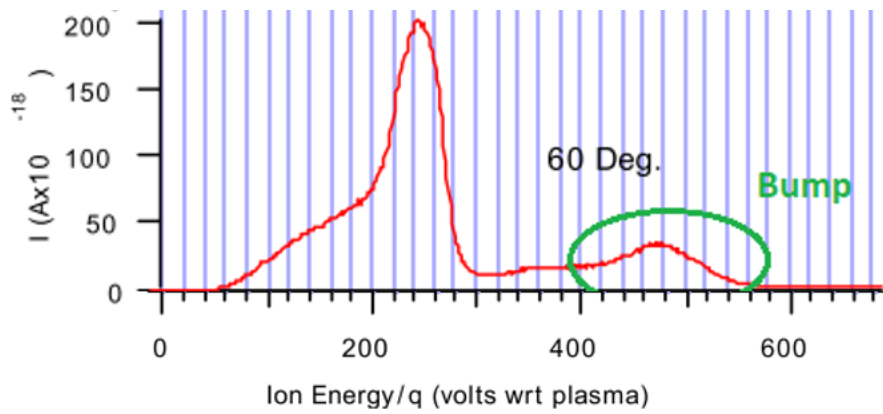
Figure 6.21: Ion energy distribution at 60° at 0.5 m from the thruster. (Ion energy/q on the horizontal axis) (King 1998)
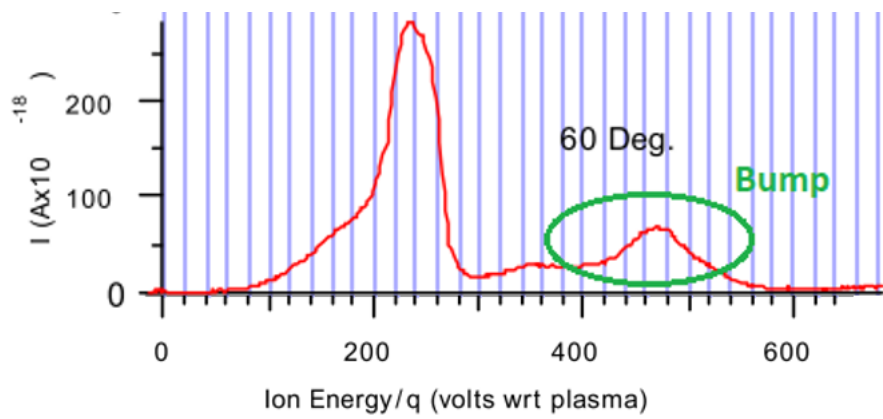
Figure 6.22: Ion energy distribution at 60° at 1 m from the thruster. (Ion energy/q on the horizontal axis) (King 1998)
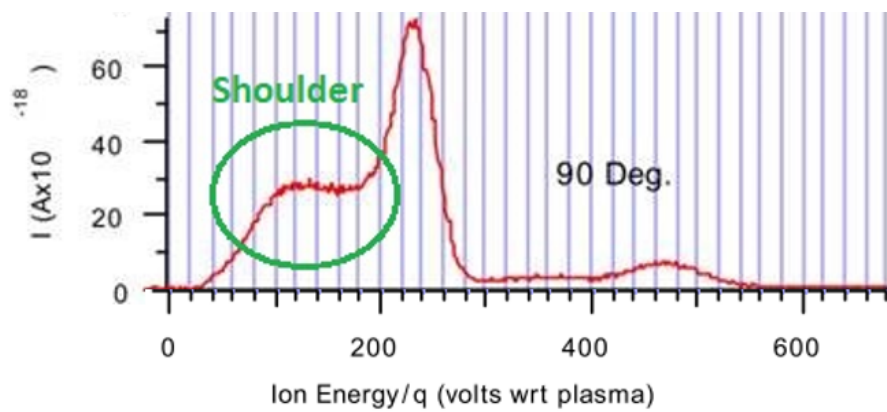
Figure 6.23: Ion energy distribution at 90° at 0.5 m from the thruster. (Ion energy/q on the horizontal axis) (King 1998)
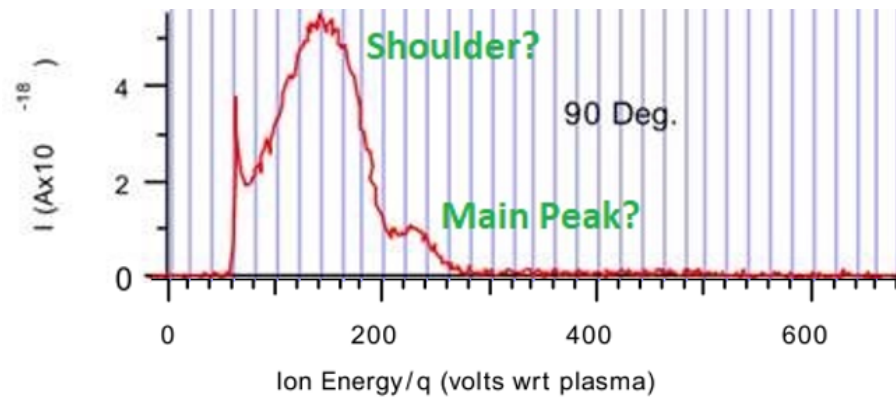
Figure 6.24: Ion energy distribution at 90° at 1 m from the thruster. (Ion energy/q on the horizontal axis) (King 1998)
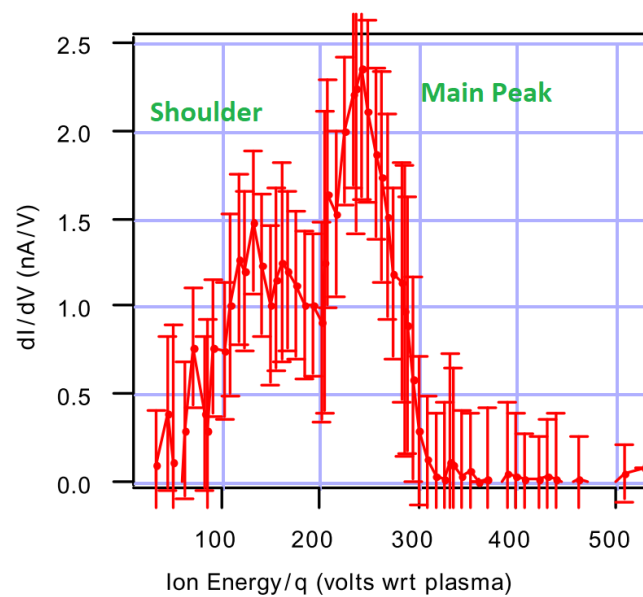
Figure 6.25: Ion energy distribution at 60° at 0.5 m from the thruster (King 1998)

Test-Facility's RPA

A second independent source of RPA measurements is the Test-Facility. Here, the most relevant feature is that at 40° angle the left hand shoulder is once again present (Figure 6.26).

6.7.3. Conclusions

Merging the knowledge gathered from RPA reading and direct measurements, it is now clear that the ions must have a double peak in the energy distribution at the exit of the discharge chamber, corresponding to the two bulks of ionization. This hypothesis is reinforced by the fact that running simulations with PICPluS with a constant ion energy distribution or a single peak distribution results in a single peak in the virtual RPA measurements.

Using the Test-Facility data as a basis, a distribution like the one in Figure 6.27 is drawn. Note that PICPluS uses as an input a function like the one shown in the lower plot. For every injected particle, a random point on the x axis is chosen and a corresponding acceleration efficiency is selected (linear interpolation in used between two specified points of the plot). The maximum number of points accepted is 20, so the points have to be optimized in order to better represent the desired function. The RPA signals produced by PICPluS and those available from the Test-Facility can be compared in Figure
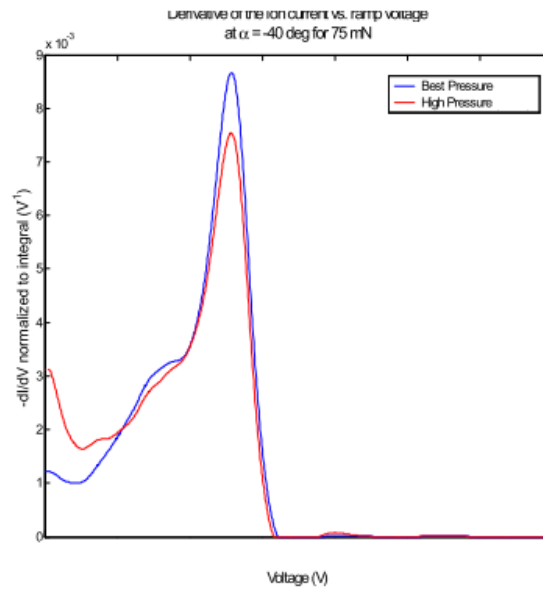
Figure 6.26: Ion energy distribution at $-40°$ at 1 m from the thruster (Confidential 2009)
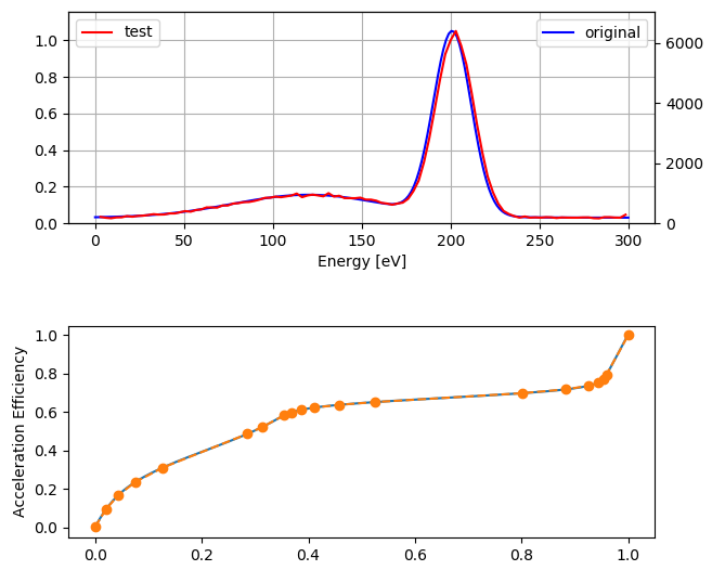
Figure 6.27: Ion energy distribution at the thruster exit (top) and correspondent input function for PICPluS with optimized points. *original* refers to the input function for the code, *test* is obtained from the plot below in order to check the exactness of the procedure (notice that is correctly coincides with the *original* function).
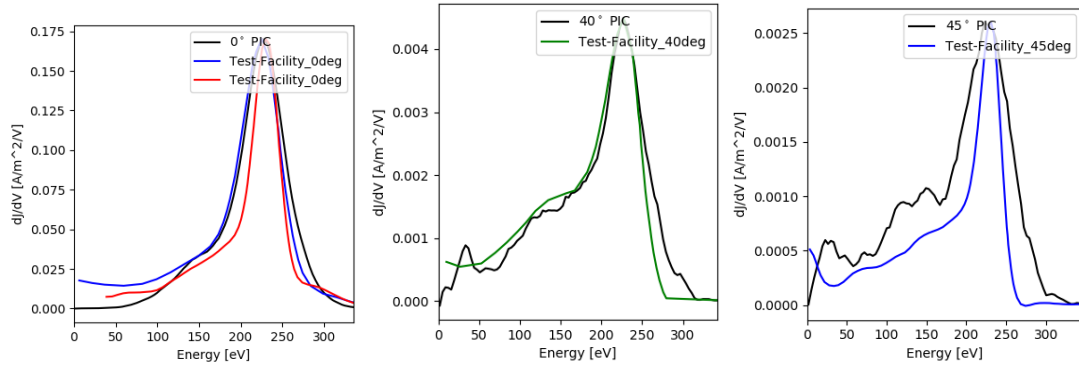
Figure 6.28: Ion energy distribution at $1\,\mathrm{m}$ according to PICPluS (black) and Test-Facility's RPA data (blue, green and red). from left to right: at $0°$, $40°$ and $45°$ from the thruster firing direction. All x and y values have been scaled by a confidential factor meant to protect OHB sensible data.

6.28. As it can be seen, a quite good resemblance is achieved. Note that the RPA data come from different testing sessions with different background pressure.

Nonetheless, some differences are still visible. In particular, at $45°$ the experimental distribution has a thinner peak and a lower shoulder. Moreover, the very low energy area seems not to match qualitatively. This behavior is peculiar, since the fit at $40°$ is much better, despite the two angular positions being very close to each other. Moreover and most importantly, at zero degrees the Test-Facility curves show a considerable amount of ions even at very low energies. While for higher angular positions low energy ions could be explained with the scattering of collision products originated in the centerline (behavior also predicted by PICPluS), this feature of the distribution at the centerline could only be explained by the generation of ions very close to the probe. This phenomena is not well understood, but it seems to be more related to the probes itself than with the undisturbed plasma. Indeed, when a mass spectrometer is used (Section 6.7.2) no ion is detected with an energy lower than a certain value. This value should correspond to the acceleration the ions undergo only outside the discharge chamber, or rather from when ionization processes are negligible.

6.8. Final Model

Making use of the knowledge reported in this chapter, a final model has been built. Figure 6.29 reports the current density and ion energy comparison with Test-Facility's data. As it can be seen, the current density gets very close to the measured one, presenting a very similar trend, only slightly underestimating the measurement. Notice that the measurement data present a deviation at $\approx 60°$. This happens only for a restricted number of data points and it is most likely caused by the interference of some object in the test chamber. The ion energy on the other hand is slightly overestimated, but once again the overall trend is respected. The RPA signal comparisons have been already shown in Figure 6.28. For completeness, the comparison with the other sets of ground data is shown in Figure 6.30, 6.31 and 6.32. A very good match persists in these cases as well. The only anomalous behavior is present in the high pressure tests ("Test-3" and "King") at the low angles ($< 30°$). This is not an issue from a functional point of view. The focus of the thesis is in fact the interaction of the plasma plume with the spacecraft structures, which are unlikely to lay that close to the engine centerline. On the other hand, this is a failure from a scientific point of view, since the model seems incapable of correctly predicting the plasma plume response to high background pressure variations for small angles from the centerline. Notice that with increasing background pressure, PICPluS estimates a lower centerline current density, since the background gas tends to lower the mobility of the injected ions. On the other hand, experimental measurements register the opposite trend. This phenomena is not yet well understood.
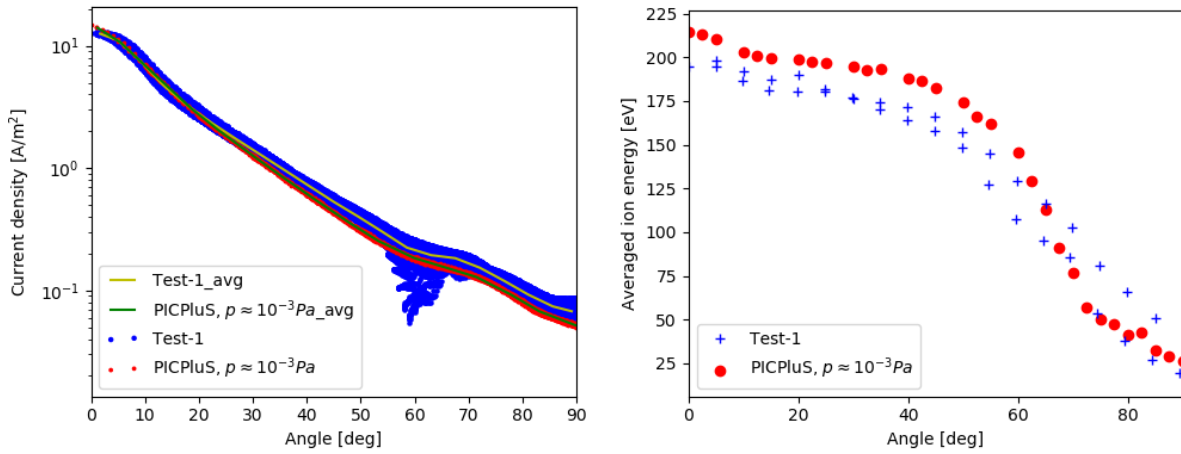
Figure 6.29: Current density and average ion energy comparison with Test-Facility Test-1. All y values have been scaled by a confidential factor meant to protect OHB sensible data.
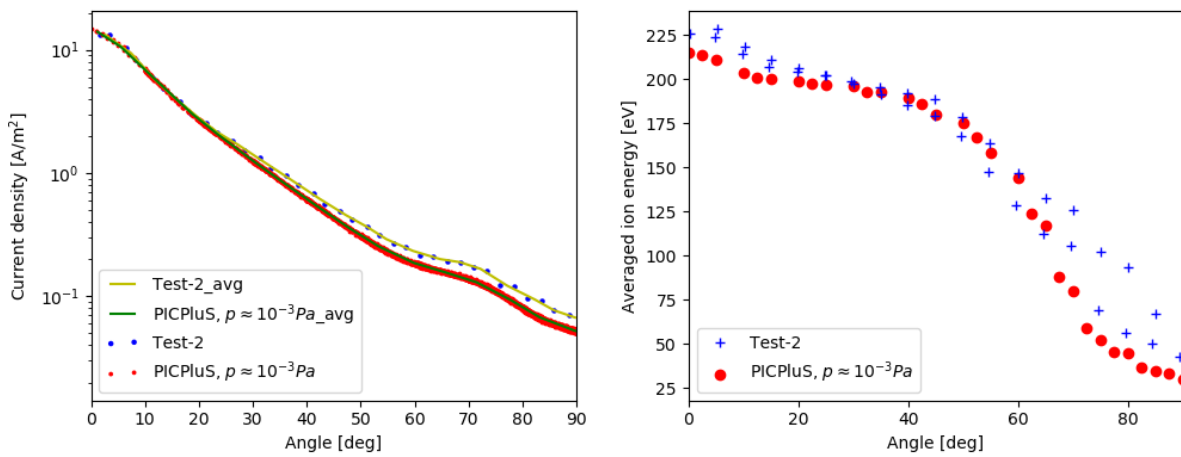

Figure 6.30: Current density and average ion energy comparison with Test-Facility Test-2. All y values have been scaled by a confidential factor meant to protect OHB sensible data.
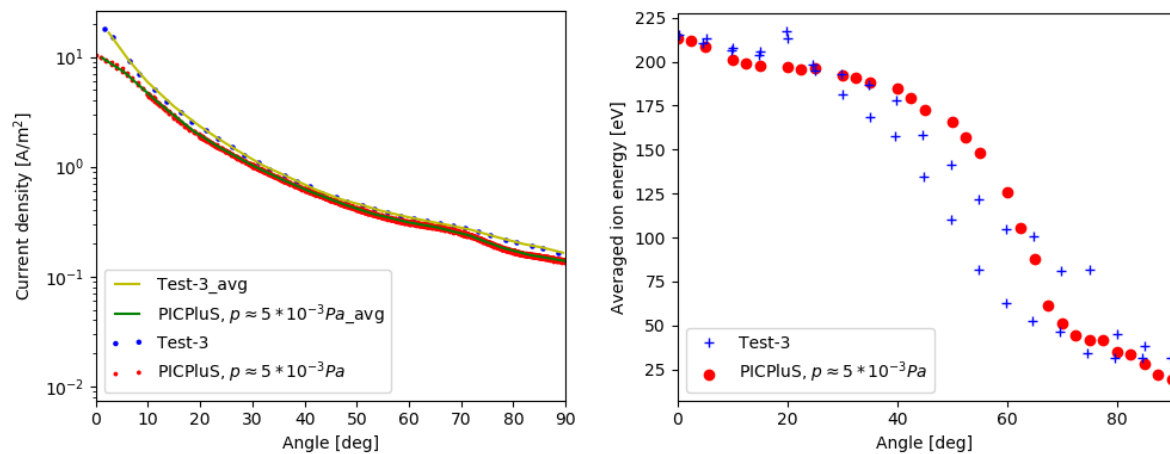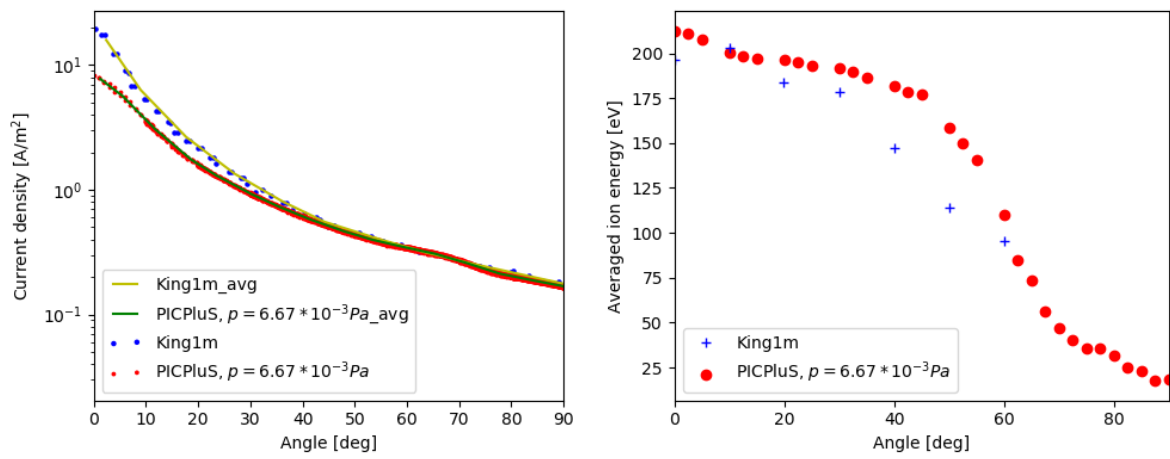

Figure 6.31: Current density and average ion energy comparison with Test-Facility Test-3. All y values have been scaled by a confidential factor meant to protect OHB sensible data.

Figure 6.32: Current density and average ion energy comparison with King. All y values have been scaled by a confidential factor meant to protect OHB sensible data.

7
Sensitivity

An important aspect of the development of a model is the sensitivity analysis. This consists in the estimation of the sensitivity of the model to a variation in the input parameters. This phase is usually undertaken at the end of a research, in order to evaluate the stability of the solution found. Nonetheless, numerous analysis have been carried out during the definition of the model, in order to assess the impact of each variable (as depicted in Chapter 6). In this chapter, though, only the sensitivity operated on the final model is presented.

To have a qualitative idea of the impact of each parameter on the output results, the following procedure has been applied:

1. Two simulations have been run with the same exact setups as the nominal ones, except for a single parameter, which has been modified by a small amount, as described in Table 7.2, both positively and negatively.

2. Current density and average ion energy plots have been extracted at 1m.

3. The relative deviation of the various plots from the nominal ones has been computed.

4. The standard deviation of the obtained values has been calculated. In the cases where the parameter has been changed both by rising and decreasing it, the average between the two standard deviations has been calculated.

The mathematical description of the last two points is given by Equation 7.1, where f is the generic value (either current density or average ion energy), f_i represent the value in the case of the incremented or decremented parameter, n is the number of sampled points and x_j the angle from the thruster centerline of the jth point.

$$impact = \sqrt{\frac{\sum_{j=1}^{n} \left(\frac{f_i(x_j) - f_0(x_j)}{f_0(x_j)} \right)^2}{n}} \tag{7.1}$$

For every parameter analyzed, two scalar numbers have been obtained (one for the current density and one for the average ion energy), indicating how much the resulting plasma is impacted. These values are shown in Table 7.1. Note that the various parameters are varied by a different coefficient depending on the nature of the parameter itself. In order to have a realistic idea on the impact of every parameter then, Table 7.2 should be taken into consideration, where the parameters variation with respect to the allowed intervals are shown. Note that only a short selection of the whole set of input parameters required by the software has been selected. All the low impact parameters have in fact been excluded from this report. Moreover, all the parameters with a clear physical and measurable meaning have been omitted (for example, the mass flow).

Parameter	Impact on current density	Impact on average ion energy
θ_i	0.119	0.138
θ_o	0.174	0.394
σ_i	0.117	0.200
σ_o	0.178	0.537
γ	0.082	0.041

Table 7.1: Parameters impact. θ_i: inner ejection angle. θ_o: outer ejection angle. σ_i: inner ejection dispersion. σ_o: outer ejection dispersion. γ: electron adiabatic coefficient

Parameter	Variation	Allowed Interval	Fraction
θ_i	10°	$-90° \iff 90°$	5.6%
θ_o	10°	$-90° \iff 90°$	5.6%
σ_i	10°	$0° \iff 90°$	11.1%
σ_o	10°	$0° \iff 90°$	11.1%
γ	0.13	$1 \iff 1.\overline{6}$	19.5%

Table 7.2: Parameters variation, allowed parameter variation interval and fraction of variation with respect to the allowed variation interval

According to Table 7.1, the angle that has the greater impact on the plasma is the outer one, with significantly more impact on the average ion energy. The dispersion coefficients (σ) have also a great impact on the plasma, comparable to that of the ejection angle themselves. Moreover, the impact is greater on the average ion energy than on the current density. Finally, the adiabatic coefficient γ has a much lower influence on the plasma than the injection angles, especially considering that this parameter has been varied significantly more than the others for this test (as shown in Table 7.2).

The method employed in this section is effective in giving a first glance at the sensitivity analysis results, but it of course does not give a full explanation on how the plasma is affected. For this purpose, the plots extracted on point 2 are hereafter analyzed. Notice that most of the observations were already described in Sections 6.3 and 6.5.

As shown in Figure 7.1, the inner injection angle has an impact on the intensity of the current density inflection point (positioned around 70°): increasing the angle the inflection point tends to disappear. Increasing this angle slightly increases also the average ion energy at high angles. This is to be expected, since a higher outer injection angle implies the spreading of the fast ions (coming out of the engine) to higher angles.

Figure 7.2 shows that the outer injection angle, like the inner one, has an impact on the intensity of the current density inflection point: increasing the angle tends to fade it. This angle has also an impact on the average ion energy at high angles from the thruster centerline, for the same reason for which the inner angle does, although much stronger.

The inner dispersion angle has a significant impact only on the average ion energy, as shown in Figure 7.3. A high inner dispersion angle provokes a higher average ion energy in the areas at high angles from the thruster centerline.

As visible in Figure 7.4, increasing the outer dispersion angle increases the current density and greatly increases the average ion energy at angles higher than $\approx 40°$.

Finally, the adiabatic coefficient seems to have very little impact on the average ion energy and current density curves, as depicted in Figure 7.5. This was already pointed out in Section 6.6.
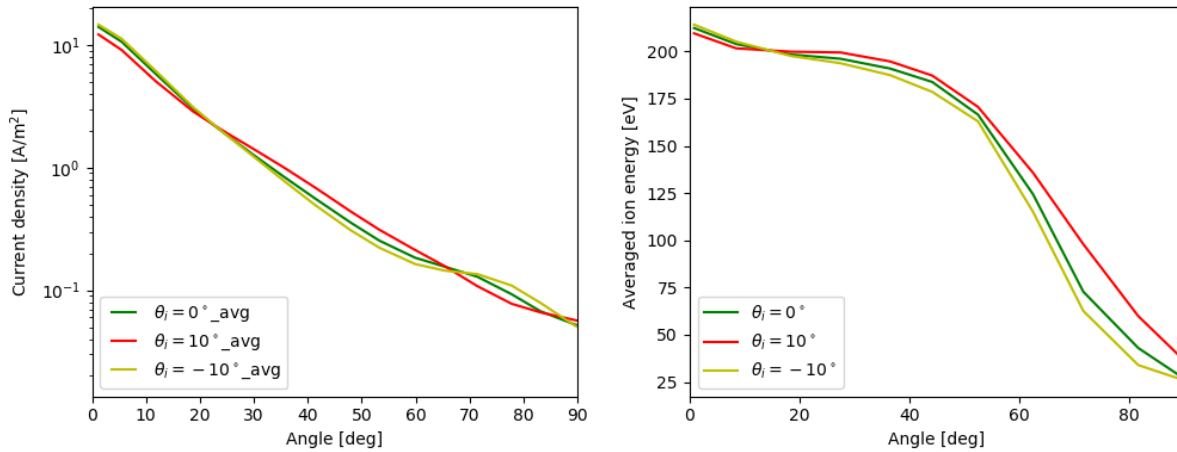
Figure 7.1: Sensitivity analysis on inner ejection angle: current density and average ion energy distributions. All y values have been scaled by a confidential factor.
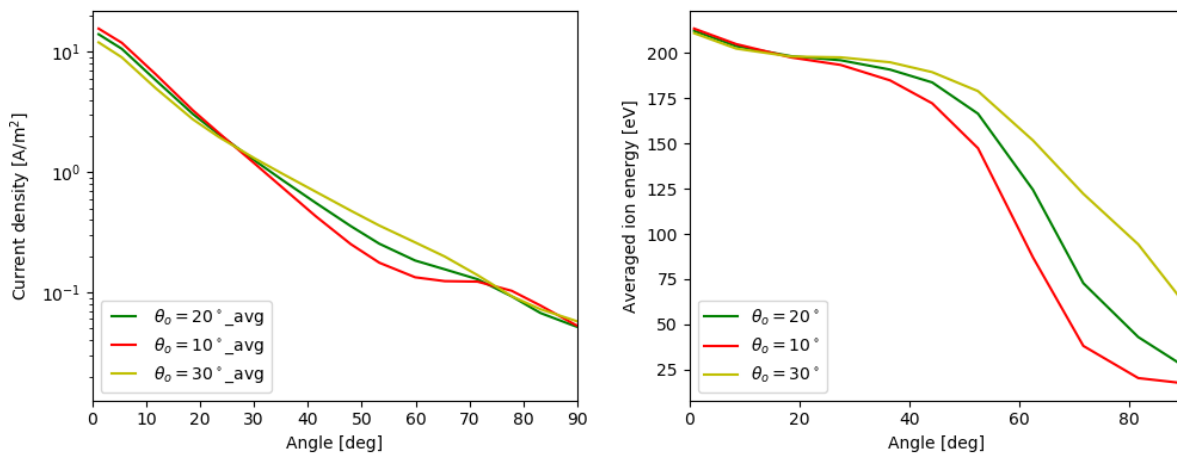
Figure 7.2: Sensitivity analysis on outer ejection angle: current density and average ion energy distributions. All y values have been scaled by a confidential factor.
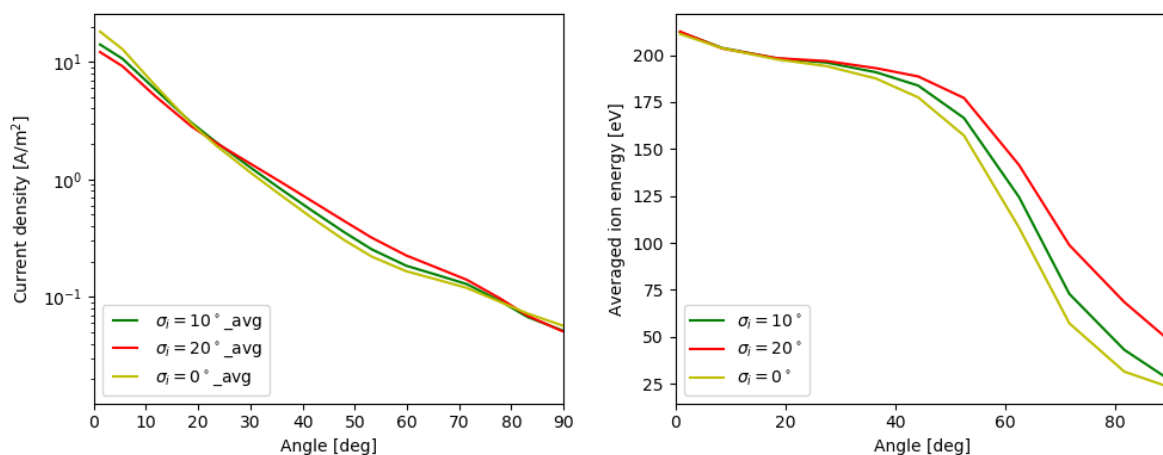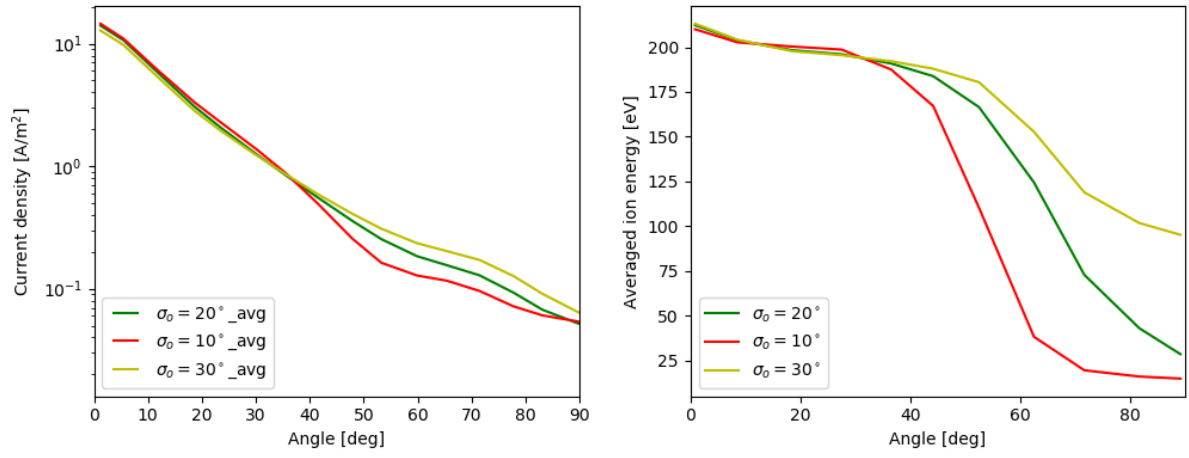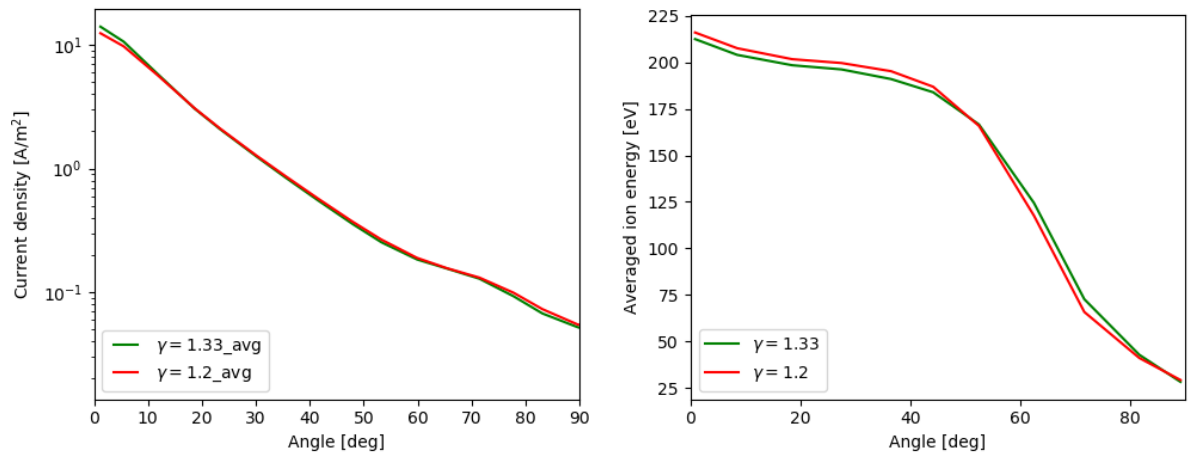

Figure 7.3: Sensitivity analysis on inner ejection angle dispersion: current density and average ion energy distributions. All y values have been scaled by a confidential factor.

Figure 7.4: Sensitivity analysis on outer ejection angle dispersion: current density and average ion energy distributions. All y values have been scaled by a confidential factor.

Figure 7.5: Sensitivity analysis on electron adiabatic coefficient: current density and average ion energy distributions. All y values have been scaled by a confidential factor.

<div align="right">

8

</div>

<div align="right">

Validation

</div>

In order to assess the ability of the model to predict the behavior of the plasma ejected by an SPT100, a number of validation cases has been set up. The set is composed by data gathered during space missions only.

8.1. Express

The first and most complete set of data comes from the Russian geostationary telecommunication mission Express (or Ekspress), and in particular from Express-A3 (Sitnikova *et al.* 2003) and Express-A2 (Manzella *et al.* 2001). During a span of three months, the satellite gathered data with its RPA probes. The probes on the Express-A3 were mounted on the solar arrays (see Figure 8.1) at two different radii, hence they gathered data at different angles from the thruster direction and at two different distances. Moreover, one probe was mounted on the body of the satellite in every mission, providing very high angle data. This last probe had a slightly different design than the other ones, being meant to register very low current densities.

To compare the results coming from the different probes, the distance from the thruster is assumed to have no effect on the ion energy, while the current density decreases with:

$$J(r) = J_0 \frac{r_0^2}{r^2} \tag{8.1}$$

Where r is the distance from the source, r_0 an arbitrary radius, here taken as $1\mathrm{m}$, $J(r)$ the current density and J_0 the current density at r_0. The results for ion energy and current density are visible in Figure 8.2.

The results of the validations are discussed in two separate subsections: Section 8.1.1 for the current density profile and Section 8.1.2 for the average energy profile. In the latter, the energy distribution profiles gathered by the RPAs are also presented.

8.1.1. Current Density Analysis

The current density profile matches to a good extent the one predicted by PICPluS, with the most striking observations being:

1. A cloud of points coming from Express-A3 data at high angles from the thruster presents much lower current densities.

2. At medium angles (between $20°$ and $40°$), the distribution assumed by the Express data shows a steeper decrease in current density with the angle from the thruster.
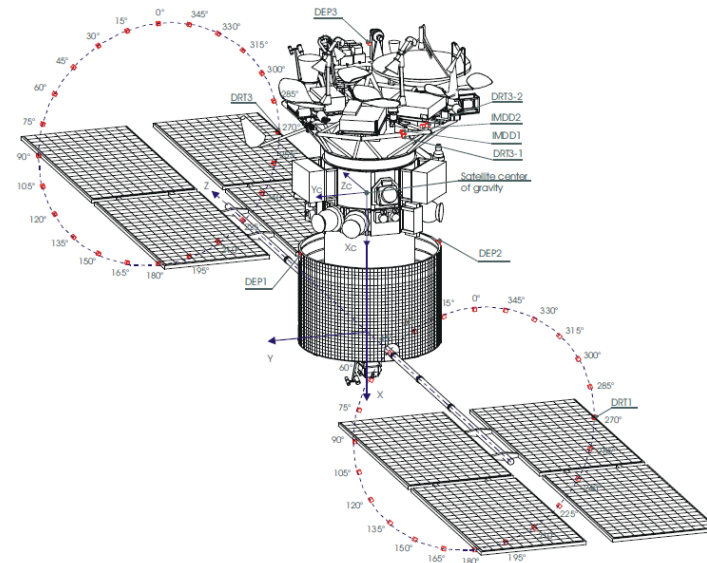
Figure 8.1: Express-A3 schematics (Sitnikova *et al.* 2003)
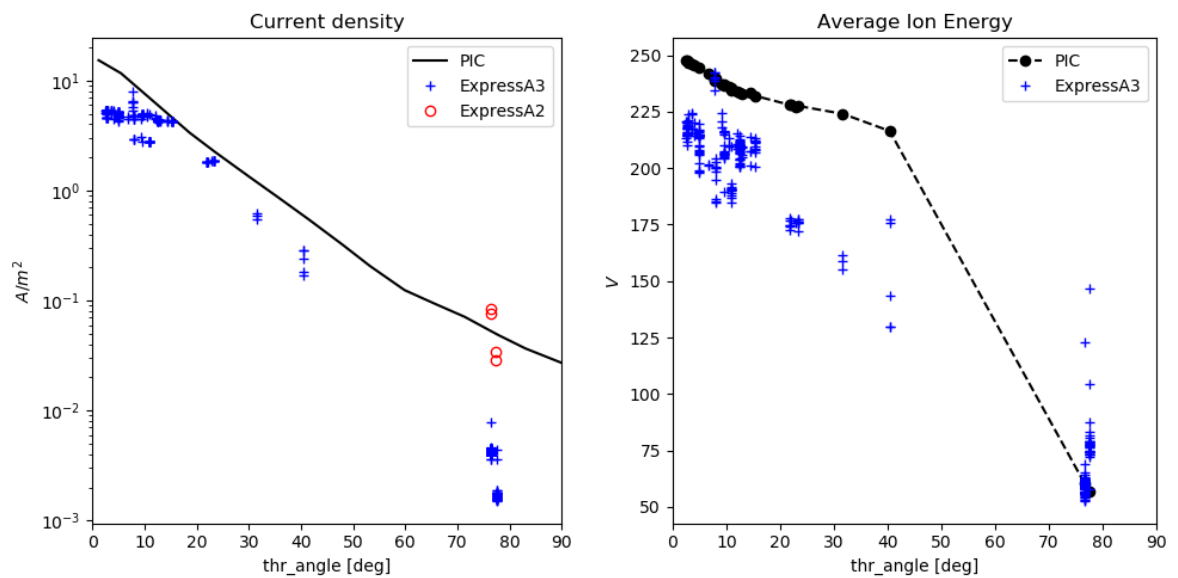
Figure 8.2: Express current density and average ion energy validation
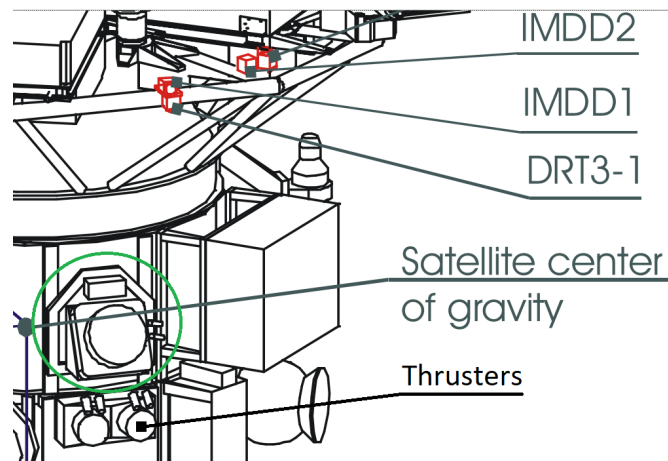
Figure 8.3: Express-A3 schematics zoomed. The probe suspected of malfunctioning is labeled DRT3-1. The potentially shadowing element is circled in green.
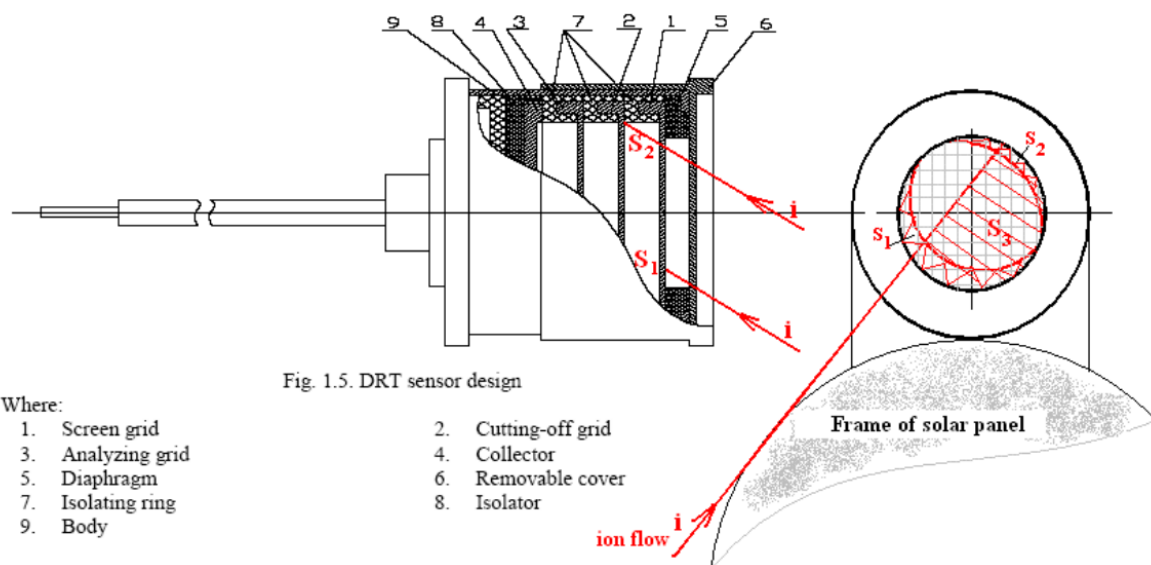
Figure 8.4: Express RPA scheme. The areas shadowed by the structure and the RPA diaphragm are shown. For a reference, the diaphragm diameter is $20mm$ wide (Korsun *et al.* 2005).

3. At low angles, the measured current density flattens, while the computed one keeps increasing when decreasing the angle.

The observation 1 can be explained by noting that the whole cloud is the result of the measurements of a single probe. The mismatch is then attributed to a probe malfunction. Another hypothesis is that parts of the structure might be laying in the line of sight of the thruster, as shown in Figure 8.3. This hypothesis can not be confirmed without a 3D model of the spacecraft.

A possible explanation for 2 is that at high angles the probes are partially shadowed by the structure of the solar array to which they are attached. In addition to this, RPA probes themselves have an angle-dependent behavior as explained in Section 2.2.2. The RPA structure is known, so a simple model can be built.

A scheme of the RPA used during the Express mission in shown in Figure 8.4. Since the geometry of the solar array structure is not known, the area of the probe shaded by it could not be computed.

When the retarding grid has a null potential, all the ions that hit directly the cutting-off grid will be
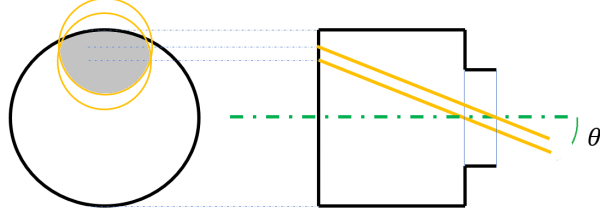
Figure 8.5: Express RPA scheme with ion-rays trajectory. The gray area is detecting incoming ions. The rest of the ions are impacting the sensor's sides. θ is the ion flow angle.
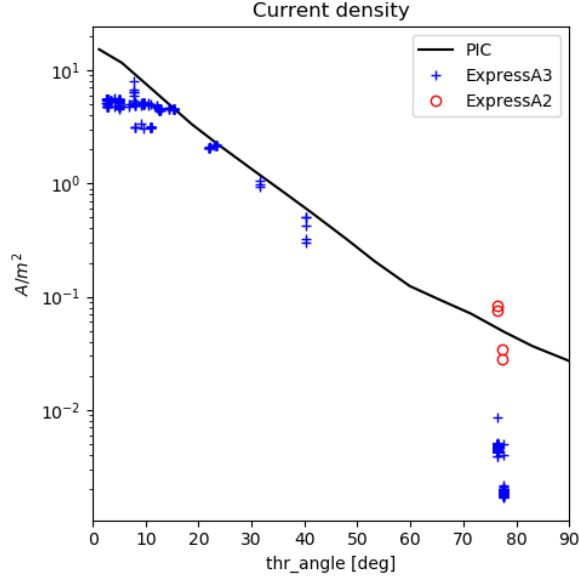
Figure 8.6: Express current density validation. Shaded areas of the RPA probe are taken into account.

detected. Those that, instead, hit the side of the probe first, will recombine with the electrons and hence do not contribute to the measured current (Korsun *et al.* 2005). On the other hand, when the retarding grid has a positive potential, the ions should also pass the retarding grid before impacting on the walls in order to be detected. If the impact happens before, in fact, the ion will loose energy and it will not be able to overcome the potential barrier. The ions that hit the cutting-off grid can be computed by assuming the ions to move in straight lines. A sketch of the effective area is shown in Figure 8.5.

The current density detected by the probes is hence corrected with:

$$J = \frac{J_0}{\cos\theta} \frac{A_0}{A_{eff}} \tag{8.2}$$

Where J_0 and J are the original and corrected current densities, respectively, A_0 is the nominal diaphragm area, θ the incidence angle and A_{eff} the area of the cut-off grid hit by the ions, as marked in gray in Figure 8.5. Note the contribute "$\cos\theta$", which takes into account the inclination of the computed area with respect to the ion flux. When this effect is taken into account, the current density is shifted as shown in Figure 8.6.

As it can be observed, although the PIC distribution still does not match perfectly the experimental one, the trend of the two curves at medium angles follows now roughly the same gradient.

8.1.2. Ion Energy Analysis
The ion energy distribution overall trend is respected, although the experimental average ion energy is much lower than the predicted one. The main reason for the discrepancy is the angle of the probe
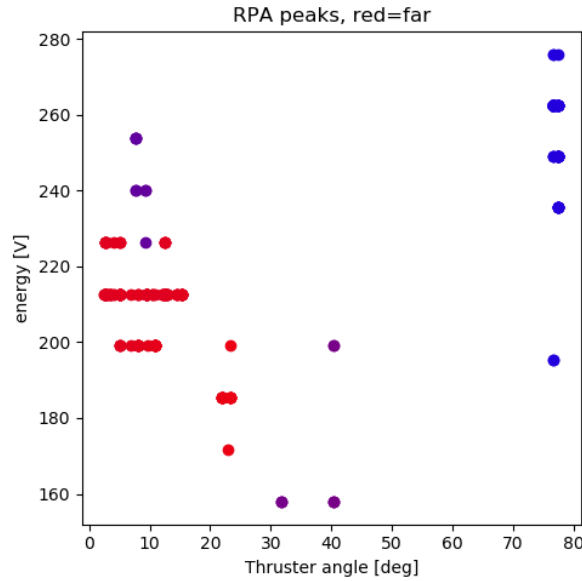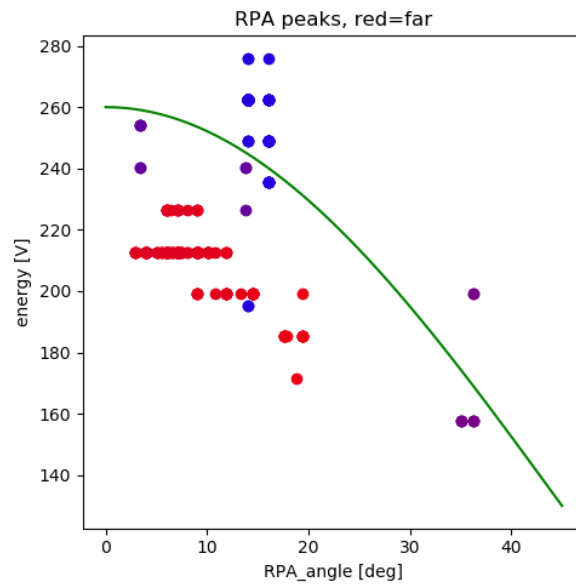
Figure 8.7: Express ion energy peak energy with respect to the thruster angle. The color indicates the distance from the thruster: red dots are further than blue ones.

with respect to the ion flux. This phenomena is clear when the RPA data are observed. According to PIC simulations in fact, the main peak of the distribution (the energy possessed by the greatest amount of ions) should be independent from the angle with respect to the thruster. The experimental data present instead a decreasing behavior, as shown in Figure 8.7. Here, the trend should be appreciated only within data coming from the same distance from the thruster (hence dots of the same color).

The dependency of the peak energy with the probe angle with respect to the ion flux is shown in Figure 8.8. In the same figure, a trend dependent on $\cos^2\theta$ is shown in green. This trend has already been hypothesized in Section 2.2.2, where the relationship between ion kinetic energy and ion perpendicular kinetic energy has been derived (Equation 2.7).

Due to the high scattering of the data, it is not possible to assess with certainty whether the supposed trend is the one registered by the RPA probes on-board the Express-A mission. Nonetheless, the correction factor is implemented, since it seems theoretically reasonable and it follows the experimental data. The average ion energy trend corrected as explained is shown in Figure 8.9.

The average ion energy trend is now much closer to the one predicted by PICPluS. The experimental energy is still lower than the predicted one. The RPA signals are now analyzed. Figure 8.10, 8.11 and 8.12 report the comparison of the RPA signals at low, medium and high angles, respectively. The energy has been corrected as described earlier in this section, while the current density correction coefficient has been discussed in Section 8.1.1. As mentioned, here it is required for the ions to hit the retarding grid before impacting the walls. The full RPA validation results are reported in Appendix A.

In the figures a certain difference is visible between the two sets. At low angles, the ion energy peak not only is misplaced, but it is also much thinner. At medium angles, the ion energy distribution roughly corresponds with the predicted one. The overall trend of the high angles data is similar, but the Express data present a much higher low energy peak. Moreover, Express data still present a small peak roughly at the same position as the main peak detected at lower angles.

In order to explain the mismatch at low and high angles, a few possible explanations are given:

1. The probe angle with respect to the ion flow is never $0°$. In the only case where this is very small, the ion energy distribution presents a main peak with a much higher energy, very close to that of the prediction, as illustrated in Figure 8.13. To take into account a generic incoming angle, the model shown in Section 2.2.2 has been applied. This model is very simple and possibly does not describe properly the phenomena.

Figure 8.8: Express ion energy peak energy with respect to the probe angle. The color indicates the distance from the thruster: red dots are further than blue ones. In green, the theoretical energy trend.
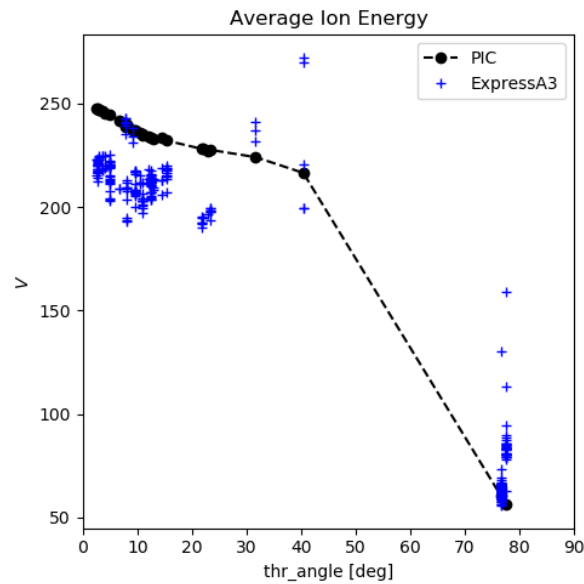

Figure 8.9: Express average ion energy data with respect to the thruster angle, corrected with a $\cos^2 \theta$ coefficient
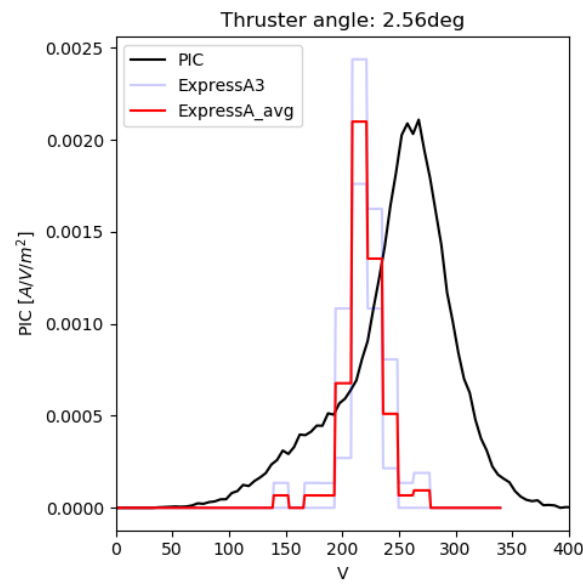
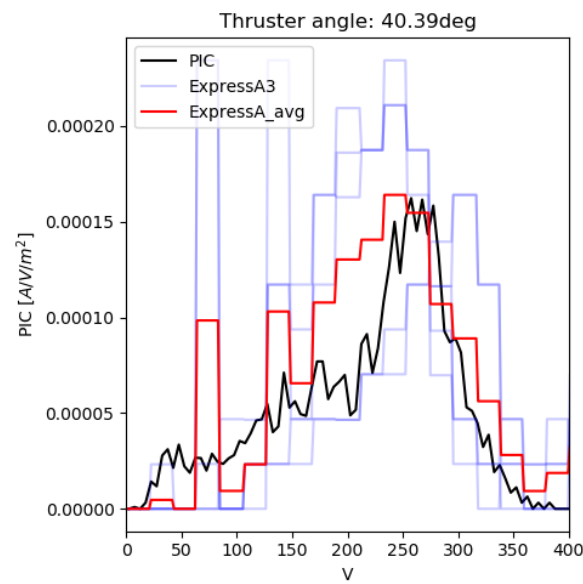Figure 8.10: Express RPA validation, data at 2.56°

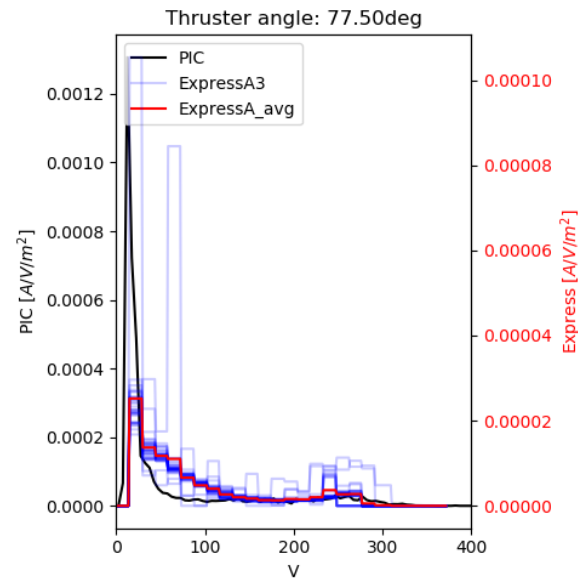Figure 8.11: Express RPA validation, data at 40.39°
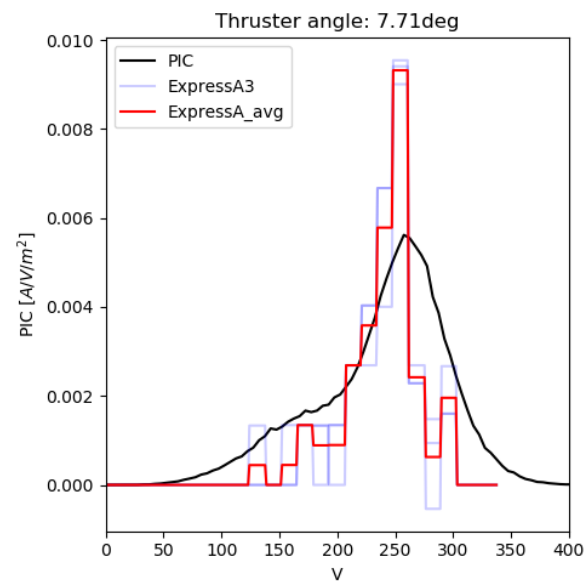
Figure 8.12: Express RPA validation, data at 77.52°

Figure 8.13: Express RPA validation, data at 7.71°

2. The electric reference system from which the RPA probes grid potential is measured is different. This would shift all the curves sideways.

3. The presence of the structure alters the ion energy distribution. This explanation would work for medium angles, since it is possible that the high energy ions are shadowed while the low energy ones bend behind the structure and hit the probe anyway, but does not properly explain the mismatch at low angles. This could both alter the current density, hence changing the curves vertical size and shift them sideways.

4. The ions actually have a different energy composition. Specifically, since the left-hand shoulder seems not to appear, the discharge chamber might have a single ionization bulk. A different ionization process in the discharge chamber can alter significantly the shape of the measured ion distributions. On turn, this could have been cause d by:

   (a) The perfect vacuum conditions alter the discharge chamber plasma generation processes.

   (b) A different SPT100 model (or a different setup) has been used during the Express mission (with respect to the on-ground Test-Facility test session).

8.2. SMART-1

The second set of validation data comes from the European mission SMART-1 (Small missions for Advanced Research in Technology-1). Here, a single diagnostic kit is placed on the side of the satellite and an RPA has collected the ion energy distribution. The quantity of data is then limited since the measurements were taken in a single spacial point at $110°$ for the thruster firing direction. Moreover, the engine employed was not the SPT100 but the PPS1350, which design is very similar to that of the SPT100 (Estublier 2008). The operating point of this thruster is shown in Table 8.1.

Thrust	70mN
Current	3.8A
Mass flow	$4.2\frac{\text{mg}}{\text{s}}$
Discharge voltage	350V

Table 8.1: PPS1350 Working conditions (Tajmar *et al.* 2004)

Once again, the body of the satellite has not been modeled. The RPA results are shown in Figure 8.14.

As it is quite clear from the plot, the SMART-1 curve is very similar to the simulated one. Notice that only the shape and horizontal displacement of the curves should be appreciated, since the SMART-1 curve has been scaled in order to match the PICPluS curve height. This has been dictated by the fact that while the ion distribution is available, the actual current is not. The experimental distribution shows the presence of ions at very low energies (below $10V$), while the model does not. This phenomena has already been observed in Section 6.7.3 and was attributed to some probe-related issue. Notice that this could also have been caused by a wrong estimation of the cathode reference potential. The raw data have in fact been shifted sideways by $18V$ in order to compensate for it (Alenia-Laben and Spa 2005), but this value could be imprecise. At energies higher than $40V$ the model underpredicts the amount of ions. This has already been observed in Section 8.1 during the Express-A mission validation at high angles. This phenomena seems to be not captured by the model and it could be given, among others, by:

1. A wrong value of the outer ejection angle and dispersion

2. A wrong value of the adiabatic coefficient

3. The interaction with the structure: due to the low energies involved, spacecraft surfaces charging could play a role
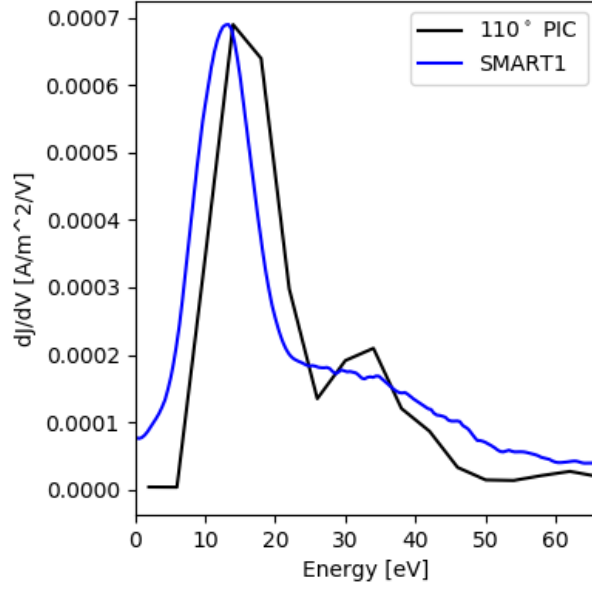
Figure 8.14: SMART-1 validation. The SMART-1 curve's peak's height is pinpointed to the simulation's peak's height

   4. This phenomena could simply be an artifact given by the little amount of ions reaching the artificial probe. A more lengthy simulation could compensate for this.

8.3. OHB-sat

The last validation set of data comes from an OHB mission, called OHB-sat. Here, two full years of parasite torques data are available. The satellite is equipped with 8 thrusters (all identical SPT100) that were used alternatively (half of them are redundant thrusters). The maneuvers were performed every day when the satellite was positioned at the same position in a sideral reference system. This means that the Sun position with respect to the satellite varied smoothly every day, and hence the solar array position with respect to the thruster at the time of firing.

   The issue with this kind of computation is that the applied torques are not a direct measurement of a plasma properties, and hence more factors come into play. In particular, plasma-surface interaction properties play an important role. To have a better control over these processes, part of the computation is executed with openPlumeEP. The model is set-up as described in Chapter 6 with vacuum conditions and a PICPluS simulation is run. The plasma properties (ion energy and current density) at $1m$ from the thruster are then extracted and used as an input for openPlumeEP (see Section 4.3). Another obstacle in the computation of parasite torques is that a constant bias torque is present due to the thrust vector misalignment with the center of mass. For this reason, only the oscillations with respect to the average are taken into account. The magnitude of such computed oscillation with respect to the oscillation of the in-orbit data is shown in Figure 8.15, where data from one of the eight thrusters have been collected. In formulas, the shown value has been computed with:

$$f(T_{sim}, T_{exp}) = \frac{|T_{sim} - \overline{T}_{sim}| - |T_{exp} - \overline{T}_{exp}|}{max(T_{sim}) - min(T_{sim})} \tag{8.3}$$

   Where T_{sim} and T_{exp} are the parasite torques as simulated and experimentally evaluated, respectively. $\overline{T}_{sim}$ and $\overline{T}_{exp}$ are the average values. The dimension of the dots represent the duration of the maneuver. The complete results of the validation are not shown for confidential reasons. Figure 8.16 presents the axis convention utilized during this test.

   As it can be seen, the procedure employed manages to predict to a good degree the parasite torque oscillations caused by the solar array. The following further observations can be made:
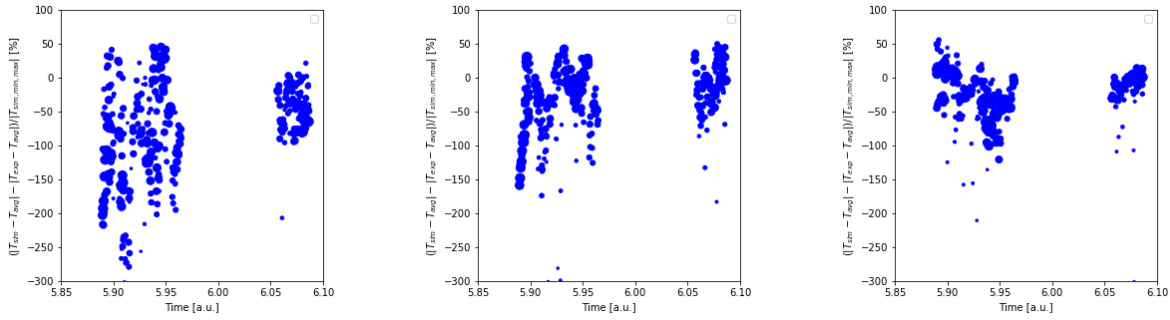
Figure 8.15: OHB-sat Validation Thruster 7. Dot dimension represents firing duration (see top left corner for reference). From left to right: torque along the x, y and z axis.
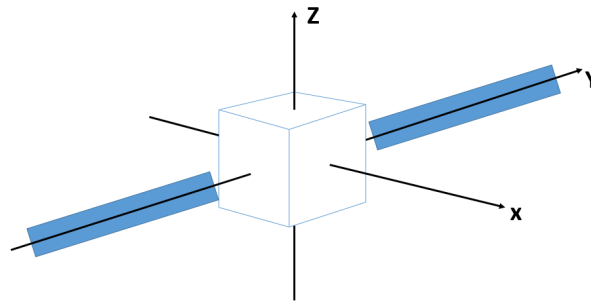

Figure 8.16: OHB-sat axis convention

1. The torque oscillations around the x axis are always underestimated

2. Shorter maneuvers present a reduction in performance

3. Some big maneuvers seem to completely mismatch the predictions and the rest of the data cloud. This effect is visible in the z torque at its best

Observation 2 is the outcome of the fact that every thruster has a transient phase of around 5 minutes at start-up. Figure 8.17 shows the recorded thrust of an SPT100 during the Test-Facility test campaign (Confidential 2009) (on-ground). Here, the transient phase is clearly visible.

Observation 3 shows a quite peculiar phenomena not yet understood. The maneuvers seem to be connected to some sort of extraordinary functioning, since the dots are usually colored differently from the rest of the cloud, and hence the maneuvers were not performed at the usual point in the orbit.

All considered, Observation 1 seems to be the only one connected to the physics involved in the simulations. More investigation on the x torque is then performed. In particular, the following can be observed:

1. All the thrusters present an underprediction and of the same order of magnitude.

2. The most relevant portion of the solar array for the x torque is the one closest to the thruster. The torque is in fact proportional to the density of the impinging ion flow on the solar array and to the distance in the y direction from the center of mass, hence to the location of the solar array along its axis, with the current density decreasing more steeply than the lever arm rising.

It is still not clear whether the error comes from the PICPluS model, the openPlumeEP approximation or the equations used to compute the plasma-body interactions. Notice that when the accommodation factor (see Section 4.3) is set to 0.6, the results improve drastically. For instance, the same thruster of Figure 8.15 now gives the plots in Figure 8.18. Nonetheless, as already mentioned in Section 4.3,
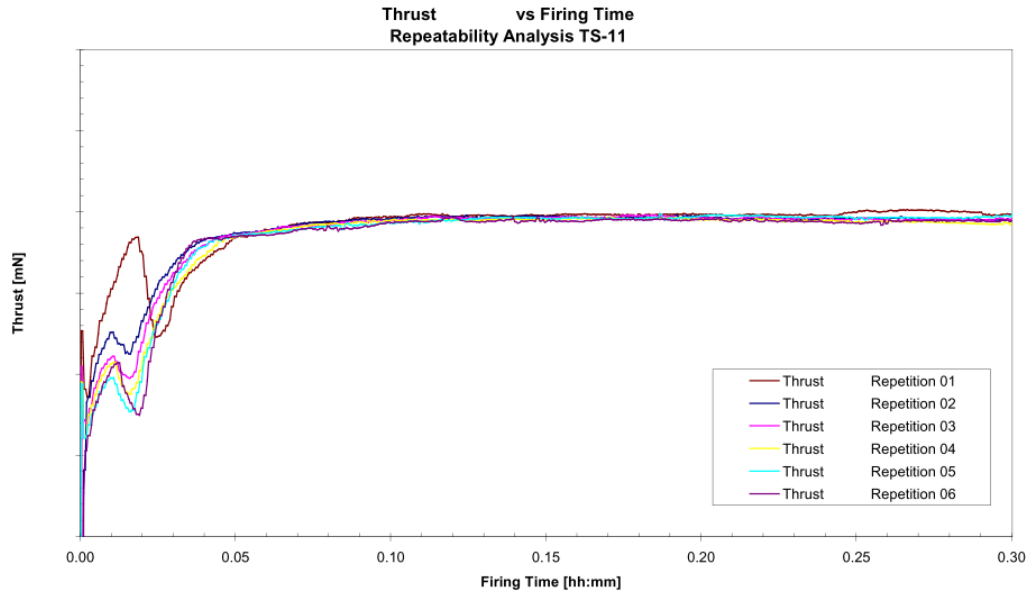
Figure 8.17: SPT100 thrust, on-ground test by the Test-Facility (Confidential 2009)
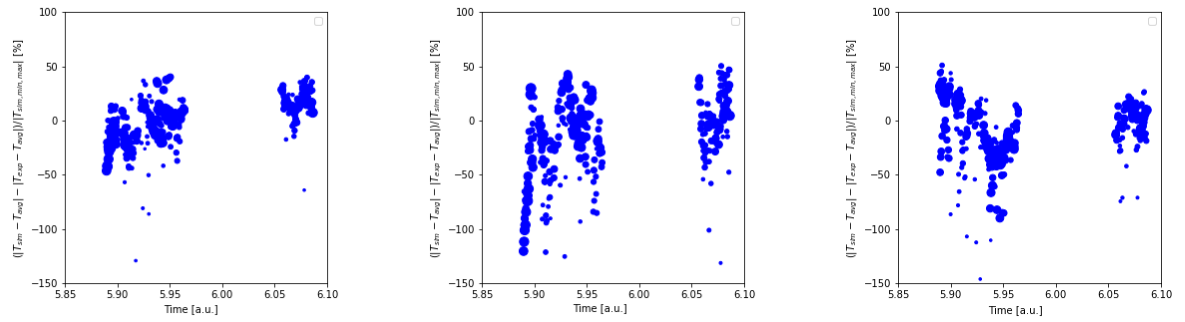
Figure 8.18: OHB-sat Validation Thruster 7, accommodation coefficient set to 0.6. Dot dimension represents firing duration (see top left corner for reference). From left to right: torque along the x, y and z axis.

there is no further reason to adopt such value, that could be a case-specific solution. This observation should be backed by theoretical proofs or further experimental evidence to be confirmed, but it gives a hint on where the model could be improved.

9

Conclusions and Recommendations

In this work the plasma plume generated by an SPT100 has been modeled using a Particle In Cell software (Chapter 6). The model has been built using data coming from several on-ground experiments. It reproduces with a very high accuracy the average ion energy distribution and the current density profile at $1\mathrm{m}$ distance from the thruster for the tuning set of data. When the model is compared with high environmental pressure tests, the central portion of the predicted plume (the first $20°$ - $30°$) underestimates the real one by a factor of 2. According to the software results in fact, at a higher background pressure should correspond less current in the centerline of the plasma plume. The opposite is instead observed in the ground data. It is then evident that the change in background pressure influences not only the presence of neutrals in the space between the thruster and the probes, but also the physics inside the thruster. The entity of such change is yet to be investigated. With these pressure conditions, the average ion energy profile is slightly overpredicted, but the differences are limited. The ground tests ion energy profiles yield good agreement with the predicted ones, showing that the model correctly interprets the ionization mechanics happening inside the thruster, as discussed in Section 6.8. The only major difference is the existence of low energy ions in the centerline, phenomena that is not yet understood and might be caused by some probe related error.

The model sensitivity to its parameters has been studied (Chapter 7). Some parameters have been recognized to be more influential than others on the plasma properties generated by the model. In particular, the greatest influence has been attributed to the outer ejection angle dispersion coefficient, the outer ejection angle and the inner angle dispersion coefficient. On the other hand, the adiabatic coefficient used to model the electron expansion properties has been found to be of less importance.

The model has then been tested on in-orbit data, proving its capability of predicting the plasma behavior in the operational conditions of an SPT100 (Chapter 8).

In the validation with the Express-A mission (Section 8.1), the model overestimated the current density by a maximum factor of 2, but showing a similar trend. Part of the mismatch is explained in Section 8.1 and attributed to the shadowing of the probes by parts of the satellite, although this factor can not be quantified. The RPA comparisons showed that the ion energy is overestimated by the model by an order of $40V$. As explained in Section 8.1, this could be given by the fact that the RPA probes were not pointing towards the incoming flow and the applied model to correct this factor might not describe properly the phenomena. Another difference between the Express-A mission RPA data and the predicted ones is that the former do not present a shoulder on the left side of the main peak like in the ground measurements. The physical meaning of this is that the discharge chamber presents only a single ionization zone. Two of the proposed causes are the perfect vacuum conditions and the difference in SPT100 setup. In the first scenario, the difference in background pressure could have an impact on the plasma flow that propagates back into the chamber modifying position and intensity of the ionization bulks. If the two overlap, the resulting ion energy distribution would be the one detected. In the second case, it is possible that a slightly different electrical configuration has been applied to the thruster. In particular, a different electromagnets electric configuration would have generated a

different magnetic field, causing once again a different ionization configuration.

The SMART1 validation (Section 8.2) proved the capability of the model to predict the ion energy distribution at high angles from the firing direction. The distribution computed by the model is very similar to that of the in-orbit data, only underestimating the presence of ions with energies higher than $30V$. The underestimation of higher energy ions at high angles from the firing direction was also observed at high angles during the Express-A validation.

The OHB-sat mission validation (Section 8.3) tested the capability of the model to predict the parasite torques applied by the plasma to the spacecraft surfaces. The only torque that shows a significant deviation with respect to the measured one is the one around the x axis. Due to the fact that the parasite torques are not a direct property of the plasma, it is very difficult to pinpoint why a difference in the results persists. The plasma-surface interaction models, for example, play an important part in this process, but have not been studied during this research.

As a result, the research question:

To which degree of precision can a hybrid particle-in-cell method as implemented by PICPluS predict in-orbit plume behavior when tuned with a non-empirical set of simulation parameters?

has been answered throughout this thesis: the current density has been predicted with a maximum deviation factor in the order of 2, while the average ion energy distribution deviation factor is in the order of 0.25. This agreement has been obtained for several different data sets, which is an indication of reliability of the model.

9.1. Recommendations

As it often happens in science, the research opened new questions to be answered by a future work. Such topics are here briefly presented.

9.1.1. RPA

The Retarding Potential Analyzers have been used to collect the data used in this research. Nonetheless, such probes tend to have errors in measurements given by shadowed regions (see Section 9.1.3), angle dependency of the transparency of the grids and secondary electron emissions (Böhm and Perrin 1993). All these phenomena are known to the scientific community, but hard to estimate and they have not been taken into account during this research. Moreover, a very simple model has been applied to compensate for the ion energy dependency on the angle. The necessity to use a more accurate model has been already highlighted in Section 8.1.

9.1.2. Low Impact Parameters

Some low impact parameters have been left out of the research, as explained in Section 6.1. These include the various species temperatures, the neutral exit angles, the percentage of doubly charged ions and the adiabatic exponent for the electron expansion model. These parameters could be taken into consideration in a future work.

9.1.3. Express Mission Validation Perfection

The Express mission data would require a more accurate pre-processing:

- As mentioned in Section 8.1, the current density registered by the probes is affected by the probe angle with respect to the ion flow. The angle has been calculated as the geometrical angle between the probe pointing and the vector connecting the thruster and probe locations. The real plasma flow angle with respect to the probe would in fact differ from this due to the curved path of the particles. Especially at high distance, this approximation should hold.

- The RPA probes tend to generate some shadow regions (Korsun *et al.* 2005), as shown in Figure 8.4. This would clearly decrease the current reaching the RPA collector, and at least partially explain why the measured currents are lower than the predictions, especially at higher angles.

- The OHB-sat validation (Section 8.3) showed how important it is to discriminate between the transient phase of the thruster functioning and the stationary phase. The thruster seems in fact to underperform in the first minutes of functioning. This aspect has not been taken into account during the Express validation. Shorter maneuvers should in fact be suppressed or be given less importance.

9.1.4. Model Generalization

The model is formed by a number of variables that are highly interconnected. Sometimes, when a working condition variable is changed, side effects generate. An already mentioned example of such behavior is the change in environmental pressure. The direct consequence is that the number of neutral particles in the domain would vary. This effect is taken into account in the model. A possible indirect effect is that the change of pressure varies the physics of the ionization processes happening inside the discharge chamber. In turn, this would vary the plasma properties. A hint of this has been shown in Section 6.8, where it has been highlighted that a change in the background pressure has the unpredicted consequence of increasing the current density at the centerline. Yet another example is that it is not clear how the discharge chamber reacts to a change in input voltage. The model used throughout this thesis scales linearly the ion energy at the exit of the discharge chamber, but this could be not exact.

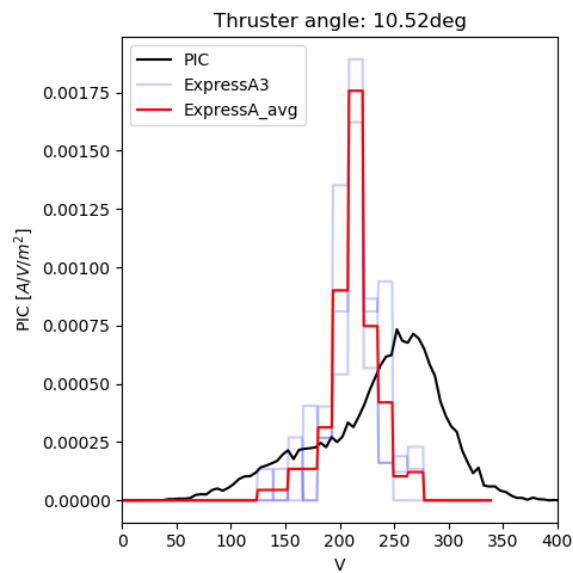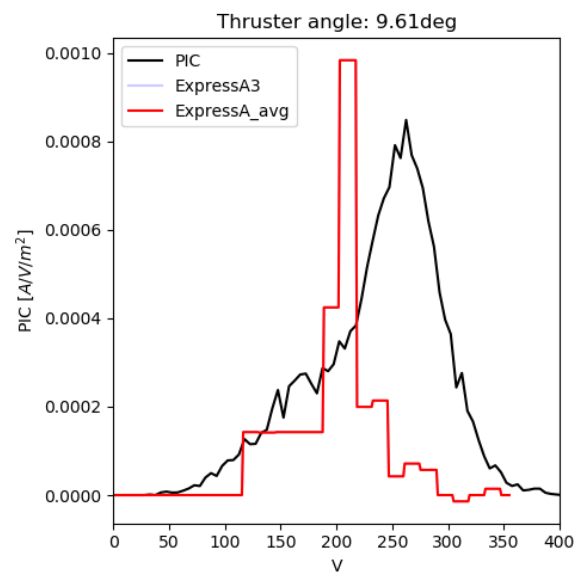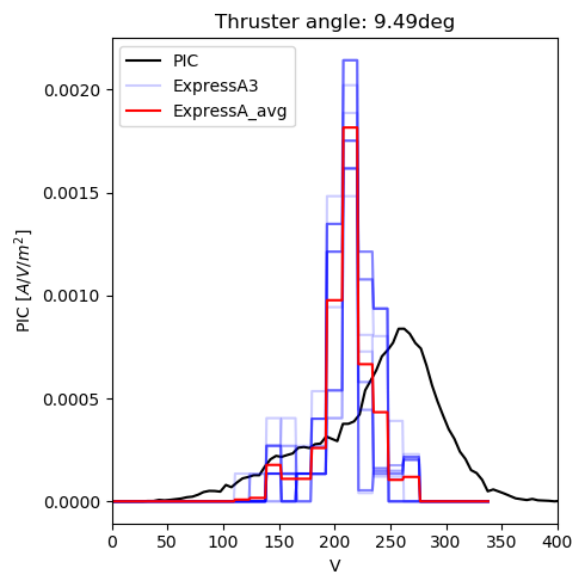In general, in order to study the side effects of major changes in the thruster working conditions, a study should be performed with more and more various data sets.
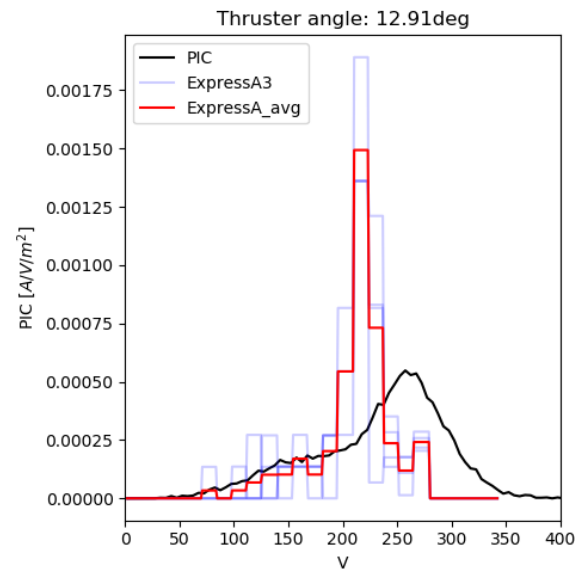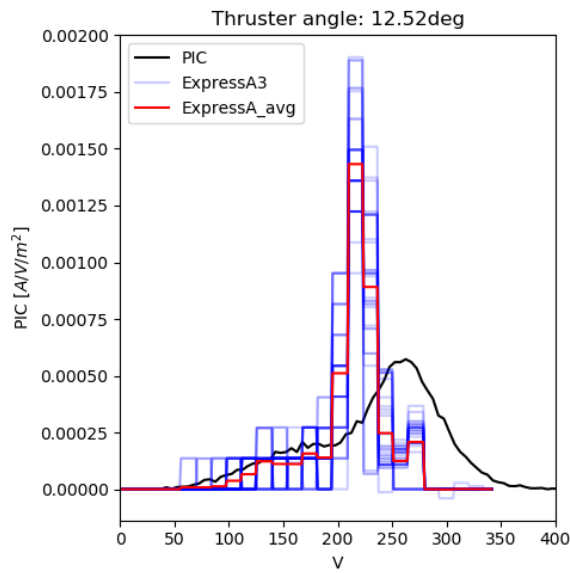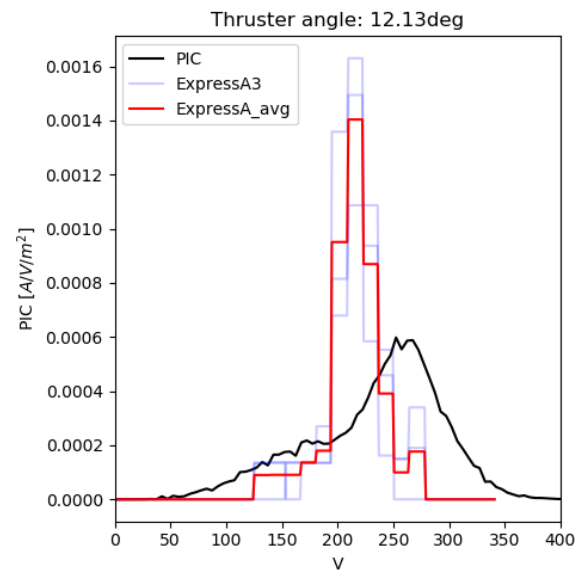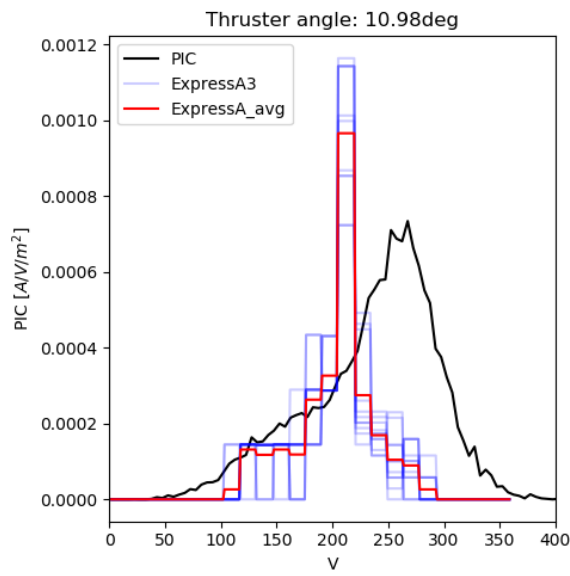
A

Express-A Validation RPA Plots

This appendix contains the complete Express-A RPA validation results.

Thruster angle: 14.43deg
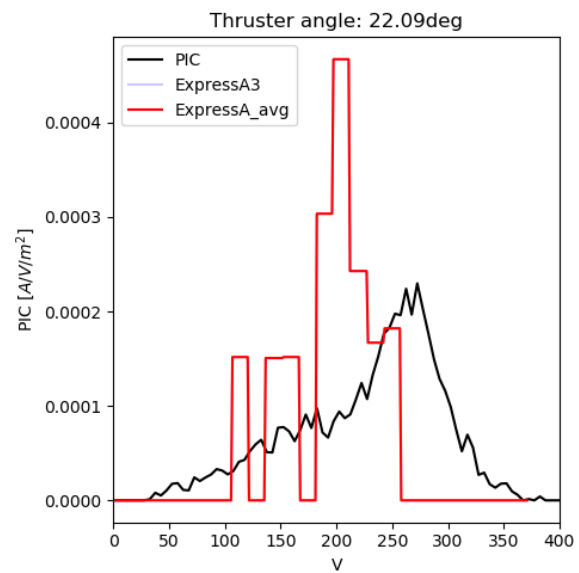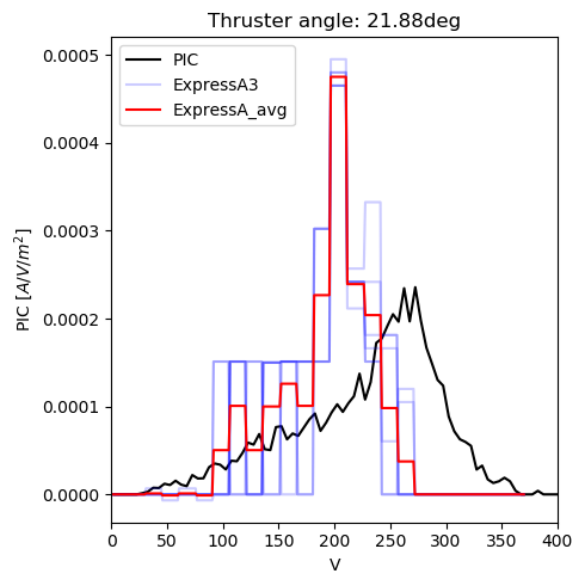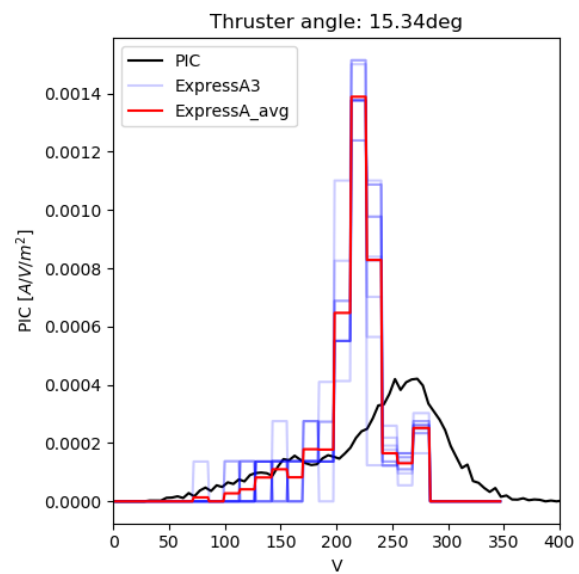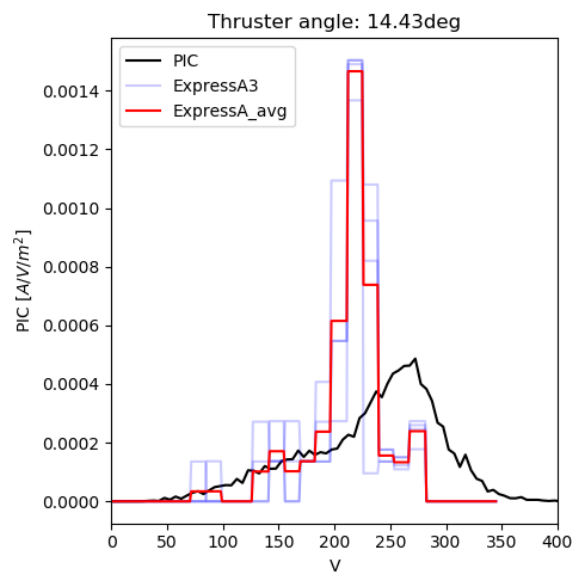
Thruster angle: 15.34deg

Thruster angle: 21.88deg

Thruster angle: 22.09deg
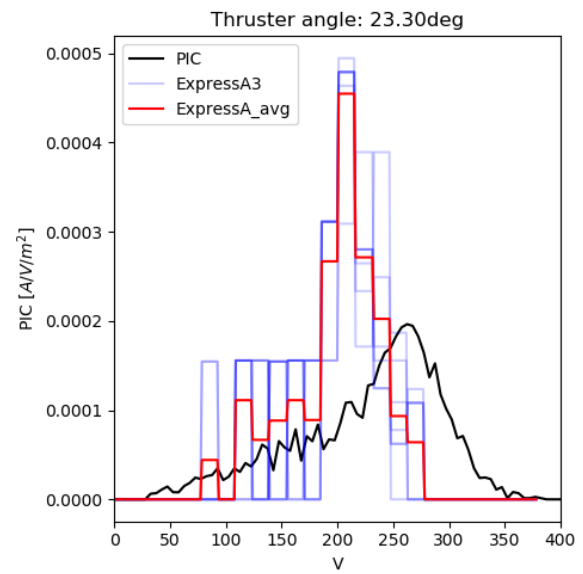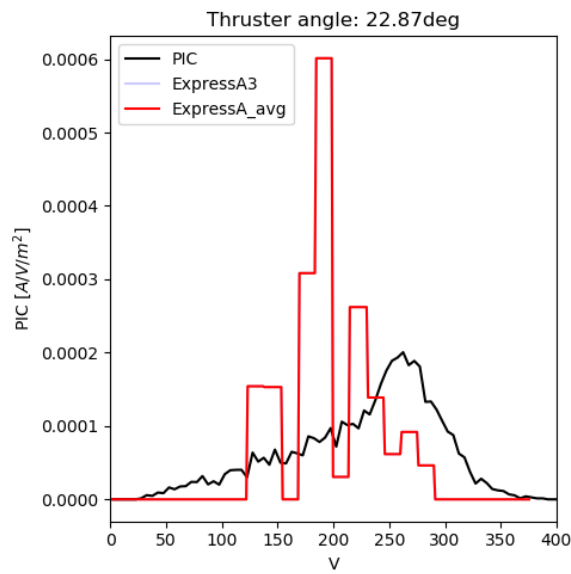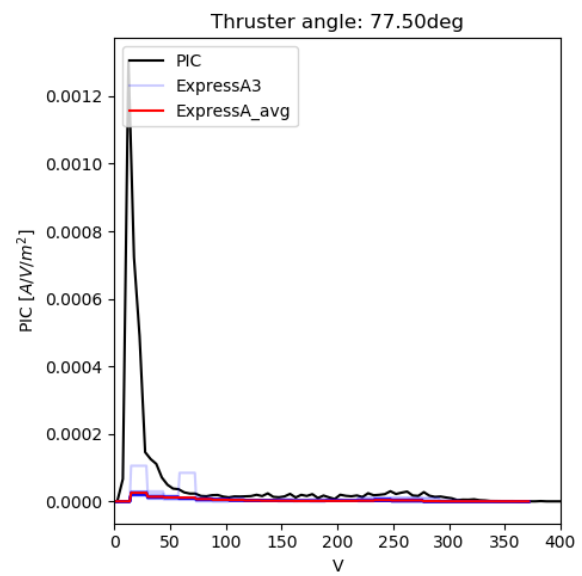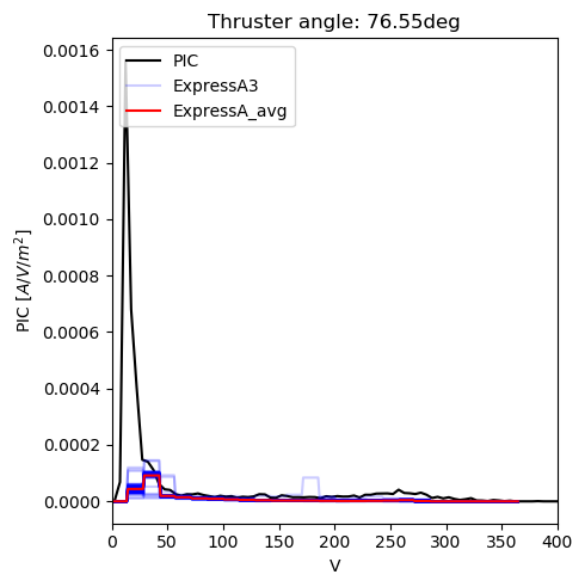
Thruster angle: 76.55deg

Thruster angle: 77.50deg
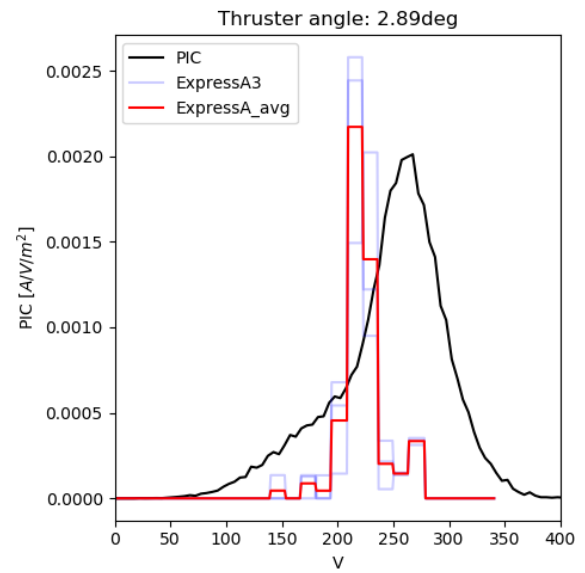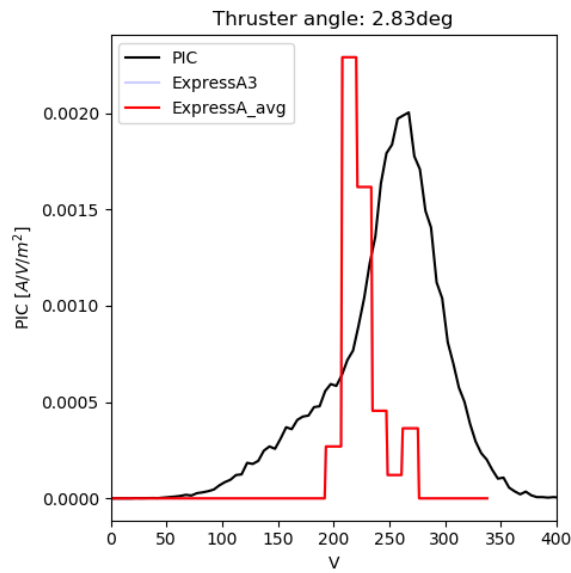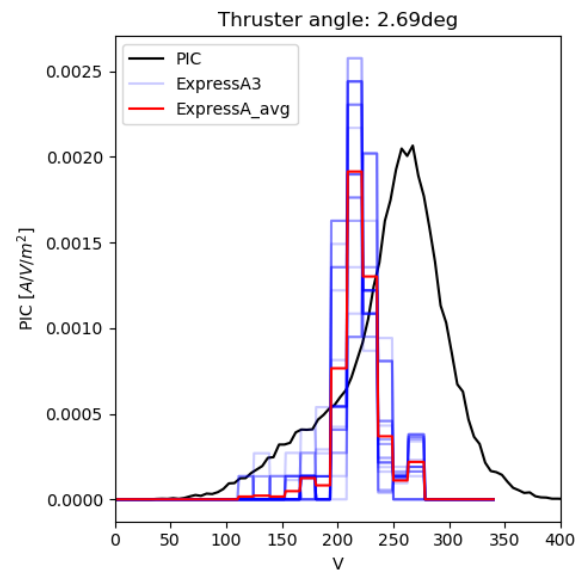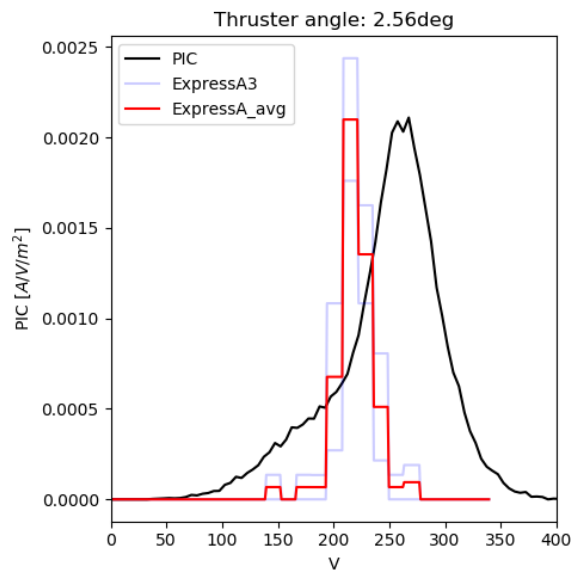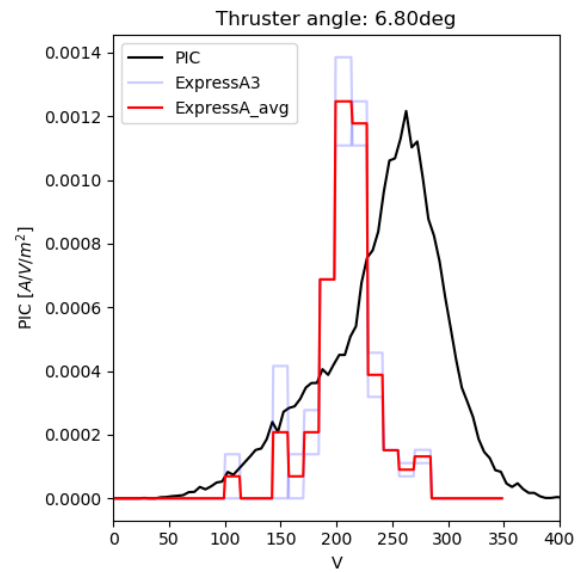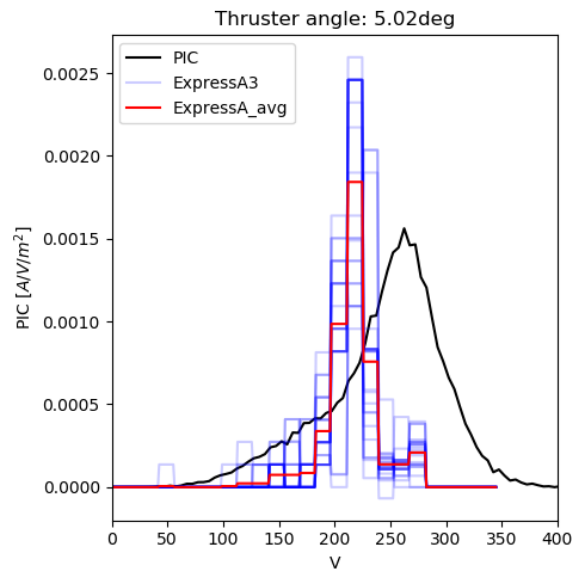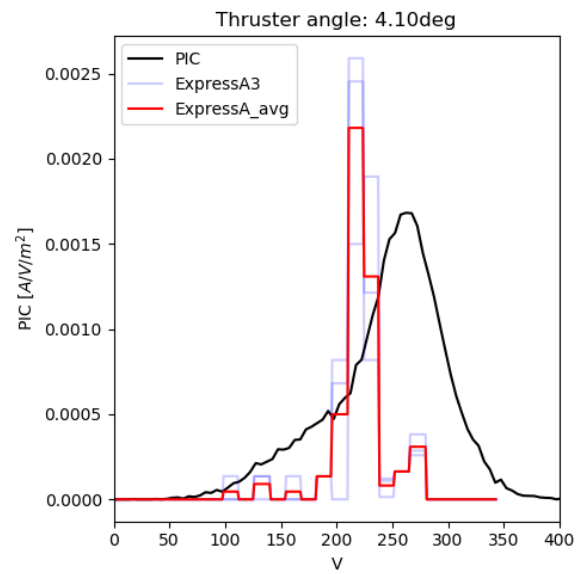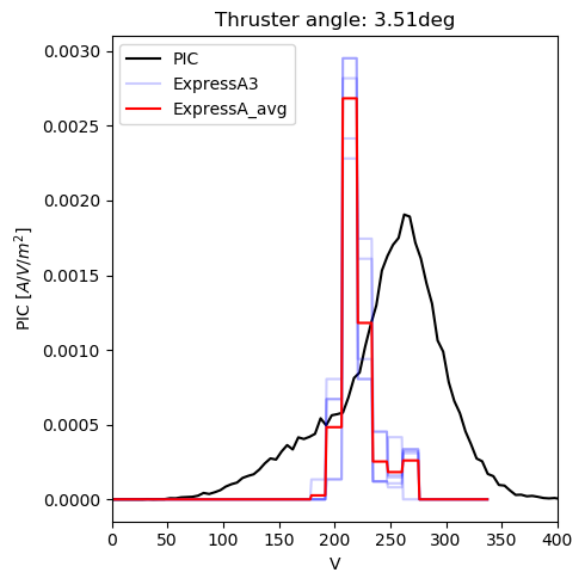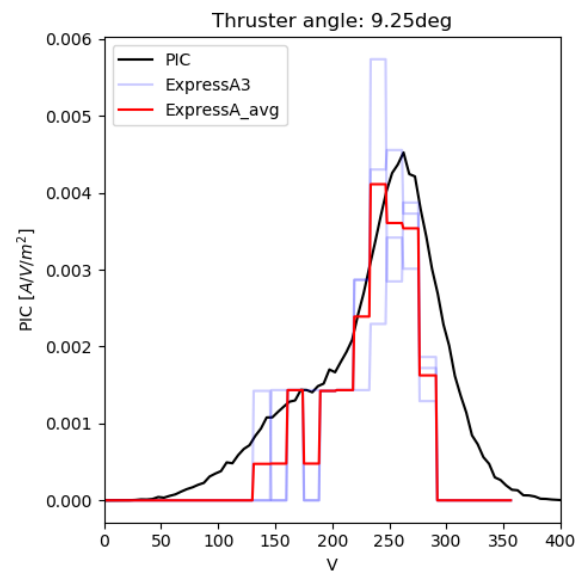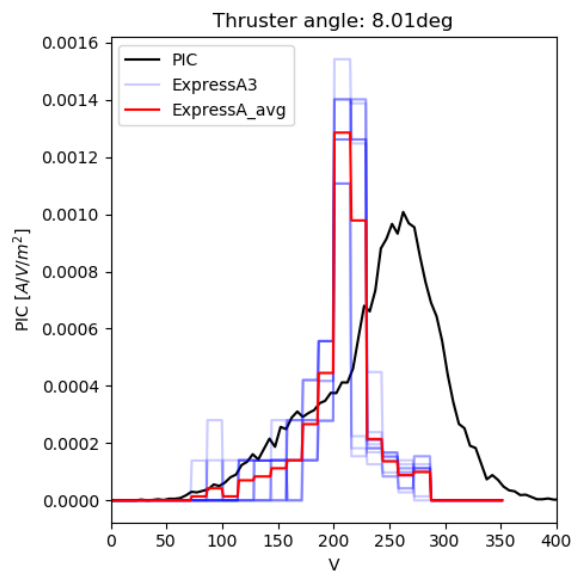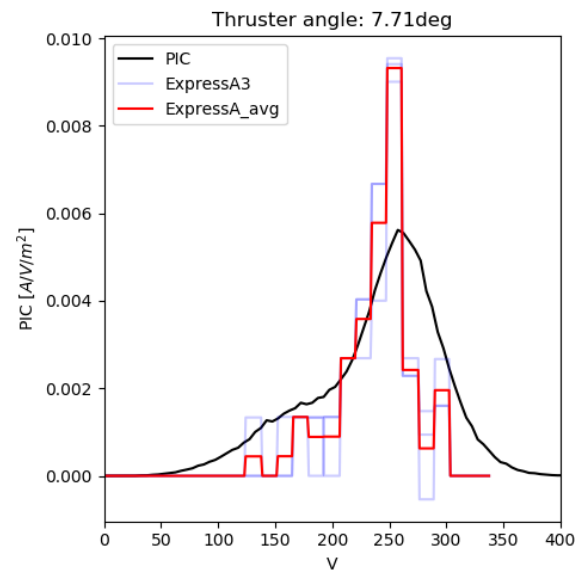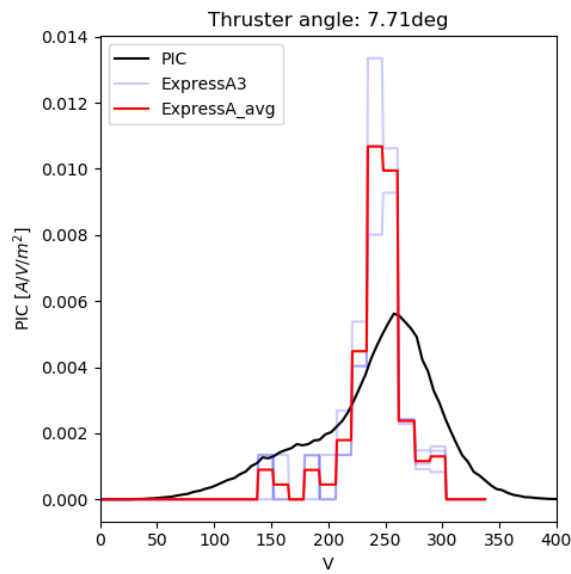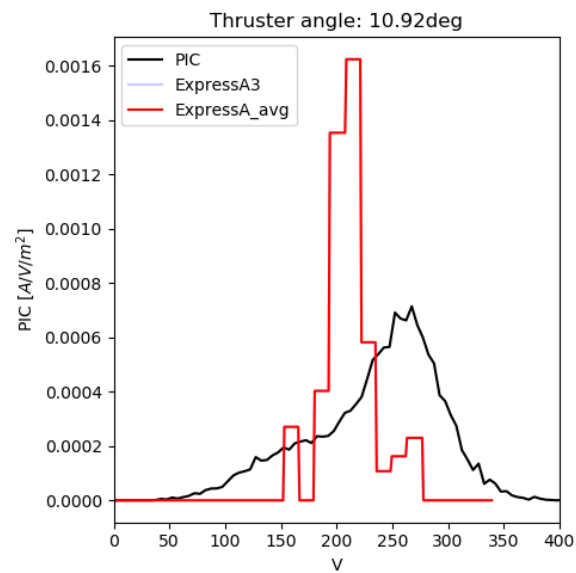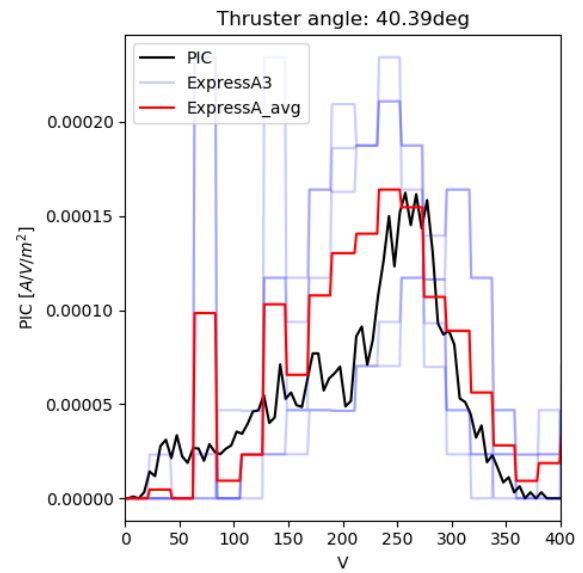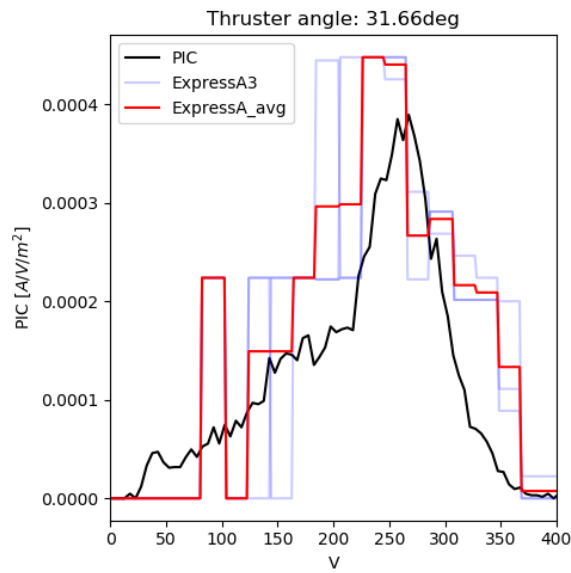
References

[1] A. R. Alenia-Laben and A. Spa, *Spacecraft/thrusters interaction analysis for smart-1,* (2005).

[2] A. G. Korsun, E. M. Tverdokhlebova, and F. F. Gabdullin, *The distinction between the ep plume expansion in space and in vacuum chamber,* in *Proceedings of the 29th International Electric Propulsion Conference* (2005) pp. 1–10.

[3] J. Likar, A. Bogorad, R. Lombardi, R. Herschitz, D. Pitchford, M. Mandell, L. Bell, and G. Kircher, *Spacecraft charging monitoring at geo: Natural and electric propulsion environment measurements,* in *47th AIAA Aerospace Sciences Meeting including The New Horizons Forum and Aerospace Exposition* (2009) p. 121.

[4] D. Fleisch, *A Student's Guide to Maxwell's Equations* (Cambridge University Press, 2008).

[5] D. M. Goebel and I. Katz, *Fundamentals of electric propulsion: Ion and Hall thrusters / Dan M. Goebel, Ira Katz*, JPL space science and technology series, Vol. 1 (Wiley, Oxford, 2008).

[6] A. Masoumzadeh, M. Habibi, and M. Afsharmanesh, *Design, construction and test of an optimized faraday cup for beam current determination of a helicon ion source,* Vacuum **159**, 99 (2019).

[7] Bolton Ferda, *Retarding potential analyzer theory and design,* (2015).

[8] L. B. King, *Transport-property and mass spectral measurements in the plasma exhaust plume of a Hall-effect space propulsion system*, Ph.D. thesis, University of Michigan (1998).

[9] A. Piel, *Plasma physics: An introduction to laboratory, space, and fusion plasmas / Alexander Piel* (Springer, Heidelberg, 2010).

[10] D. L. Kahnfeld, *Hybrid Plume Modeling*, Ph.D. thesis, Greifswald (August 20, 2015).

[11] M. J. L. Turner, *Rocket and Spacecraft Propulsion: Principles, Practice and New Developments*, 2nd ed. (2005).

[12] P. Hill and C. Peterson, *Mechanics and Thermodynamics of Propulsion*, second edition ed. (Pearson, 1991).

[13] F. McWalter, *Wfm hall thruster,* (2007).

[14] NASA/Glenn Research Center, *Russian stationary plasma thrusters,* (1997).

[15] Alessandro Vicini, *Picplus v.3.6 user manual,* (18/10/2018).

[16] *Picplus v3.3 theory manual,* (04/06/2016).

[17] E. A. Bondar, V. A. Schweigert, G. N. Markelov, and M. S. Ivanov, *Assessment of cex ion backflow of spt-100 thruster,* in *AIP Conference Proceedings*, Vol. 585 (2001) pp. 278–284.

[18] K. Dannenmayer and S. Mazouffre, *Electron flow properties in the far-field plume of a hall thruster,* Plasma Sources Science and Technology **22**, 1 (2013).

[19] B. Zitouni, V. Sonneveld, and N. Massaccesi, *openplumeep,* (2018).

[20] L. King and A. Gallimore, *Ion energy diagnostics in the plume of an spt-100 from thrust axis to backflow region,* in *34th AIAA/ASME/SAE/ASEE Joint Propulsion Conference and Exhibit* (1998) p. 3641.

[21] D. Manzella and J. Sankovic, *Hall thruster ion beam characterization,* in *31st Joint Propulsion Conference and Exhibit* (1995) p. 2927.

[22] Confidential, *Spt100 plume test report to ohb number 1,* (2009).

[23] D. Manzella, *Stationary plasma thruster ion velocity distribution,* in *30th Joint Propulsion Conference and Exhibit* (1994) p. 3141.

[24] N. Loureiro, *Modelling of plasma thruster plumes for spacecraft-plume impingement analysis* (2010).

[25] Burm, K. T. A. L., W. J. Goedheer, and D. C. Schram, *The isentropic exponent in plasmas,* (1999).

[26] C. A. Thomas, N. Gascon, and M. A. Cappelli, *Non-intrusive characterization of the hall thruster azimuthal drift current,* AIAA (2004).

[27] J. Haas and A. Gallimore, *An investigation of internal ion number density and electron temperature profiles in a laboratory-model hall thruster,* in *36th AIAA/ASME/SAE/ASEE Joint Propulsion Conference and Exhibit* (2000) p. 3422.

[28] N. Sitnikova, D. Volkov, I. Maximov, V. Petrusevich, and D. Allen, *Hall effect thruster interactions data from the russian express-a2 and express-a3 satellites,* (2003).

[29] D. Manzella, R. Jankovsky, F. Elliott, I. Mikellides, G. Jongeward, and D. Allen, *Hall thruster plume measurements on-board the russian express satellites,* (2001).

[30] D. L. Estublier, *The smart-1 spacecraft potential investigations,* IEEE Transactions on Plasma Science **36**, 2262 (2008).

[31] M. Tajmar, B. Foing, J. Gonzalez, G. Noci, W. Schmidt, and F. Darnon, *Charge-exchange plasma contamination on smart-1: First measurements and model verification,* in *40th AIAA/ASME/SAE/ASEE Joint Propulsion Conference and Exhibit* (2004) p. 3437.

[32] C. Böhm and J. Perrin, *Retarding–field analyzer for measurements of ion energy distributions and secondary electron emission coefficients in low–pressure radio frequency discharges,* Review of Scientific Instruments **64**, 31 (1993).